1
2
3
4 **Modeling a tropical-like cyclone in the Mediterranean Sea**
5
6 **under present and warmer climate**
7
8
9
10
11
12

13 Shunya Koseki[1], Priscilla A. Mooney[2], William Cabos[3],
14 Miguel Ángel Gaertner[4], Alba de la Vara[4,6], Juan Jesus González Alemán[5]
15
16
17
18
19
20
21 *1: Geophysical Institute, University of Bergen / Bjerknes Centre for Climate Research, Bergen, NORWAY*
22 *2: NORCE Norwegian Research Centre AS / Bjerknes Centre for Climate Research, Bergen, NORWAY*
23 *3: Departamento de Ciencias Fisica, Universidad de Alcalá, Alcalá de Henares, SPAIN*
24 *4: Facultad de Ciencias del Medio Ambiente, Universidad de Castilla-La Mancha, Toledo, SPAIN*
25 *5: Departamento de Física de la Tierra y Astrofísica, Universidad Complutense de Madrid, Madrid, SPAIN*
26 *6: Departamento de Matemática Aplicada a la Ingenierá Industrial, E.T.S.I. Industriales, Universidad*
27 *Politécnica de Madrid, Madrid, SPAIN*
28
29
30
31
32
33
34
35
36
37
38
39
40
41
42
43
44
45
46
47 Correspondence to Shunya Koseki
48 Address: Allégate 70, 5007, Bergen, Norway
49 Email: Shunya.Koseki@gfi.uib.no
50
51
52
53

1

Abstract

This study focuses on a single Mediterranean hurricane (hearafter medicane), to investigate the medicane response to global warming during the middle of the 21st century and assesses the effects of a warmer ocean and a warmer atmosphere on its development. Our investigation uses the state-of-the-art regional climate model WRF to produce the 6-member, multi-physics ensembles. Results show that our model setup can reproduce a realistic cyclone track and the transition from an initial disturbance to a tropical-like cyclone with a deep warm core although the transition is earlier than for the observed medicane. To investigate the response of the medicane to future climate change, a pseudo global warming (PGW) approach has been used. This is the first adaptation of the PGW framework to study medicane. The PGW approach adds a climate change delta to WRF's boundary conditions which is obtained for all prognostic variables using the mean change in an ensemble of CMIP5 simulations. A PGW simulation where the climate change delta is added to all prognostic variables (PGW$_{ALL}$) are incremented shows that most of the medicane characteristics moderately intensify, e.g., surface wind speed, uptake of water vapour and precipitation. However, the maximum depression of sea level pressure (SLP) minimum is almost identical to that under present climate conditions. Two additional PGW simulations were undertaken; One simulation adds the projected change in sea surface and skin temperature only (PGW$_{SST}$) while the second simulation adds the PGW changes to only atmospheric variables (PGW$_{ATMS}$) i.e. we use present time sea surface temperatures. These simulations show opposite effects on the medicane. In PGW$_{SST}$, the medicane is more intense than PGW$_{ALL}$ as indicated by the lower SLP values, the stronger surface wind, and the more intense evaporation and precipitation. In contrast, the medicane in PGW$_{ATMS}$ still transitions into a tropical-like cyclone with a deep warm core, but the medicane in PGW$_{ATMS}$ weakens considerably (SLP, surface wind and rainfall decrease). This difference can be explained by an increase in water vapour driven by the warmer ocean surface (favourable for cumulus convection) and the warmer and drier atmosphere in PGW$_{ATMS}$ tends to inhibit condensation (unfavourable for cumulus convection). As a result of these counteracting effects of warmer ocean and atmosphere, the medicane is enhanced only modestly by global warming. The novel approach in this study provides new insights on the difference roles of anthropogenic warmer ocean and atmosphere in the medicane development.

1. Introduction

It is well known that severe cyclonic storms occur in the Mediterranean Sea, in particular, from September to March (e.g., Cavicchia et al., 2013). They generate large amount of precipitation and intense winds that severely damage regional economies and infrastructure over the coastal areas in the Mediterranean nations (e.g., Bakkensen, 2017). Although these cyclonic systems have a clear societal importance, methods to robustly detect these cyclones via physical criterion (e.g., Cavicchia et al. (2013) and Zhang et al. (2020)) have remained elusive (Gaertner et al., 2018). The cyclonic systems are typically detected via phenomenological criteria such as the cloud-free "eye". Consequently, most known cyclonic storms in the Mediterranean Sea develop into meso-scale cyclones with a cloud-free "eye" around the cyclone centre, which is also a common feature of tropical cyclones.

These tropical-like cyclones are called Mediterranean hurricanes or medicanes (this term is used hereafter). Although there are many similarities between medicanes and tropical cyclones, there are also clear differences between them. Firstly, the lifetime of medicanes is shorter than that of most tropical cyclones. Secondly, the development of tropical cyclones generally requires that sea surface temperatures (SSTs) exceed the empirical threshold of 26°C. However, SSTs in the Mediterranean Sea are almost never this warm with autumn and winter SSTs varying from around 18°C to 23°C in the current climate (e.g., Shaltout and Omstedt, 2014; Fig. 2a). This is thus much lower than the empirical threshold of 26°C for tropical cyclone formation and the occurrence of tropical cyclones over such cold SSTs are very rare even in the tropics (cf. Pacific and Atlantic cold tongue, e.g., Jin 1996; Caniaux et al., 2011). Another difference between medicanes and tropical cyclones is that the formation of medicanes is generally preceded by an intrusion of trough-like systems or cut-off lows over the Mediterranean (Fita et al., 2006; Chaboureau et al., 2012; Fita and Flaounas, 2018; Bouin and Lebeaupin Brossier, 2020). In particular, Fita and Flaounas (2018) suggested that some medicanes show hybrid features of tropical and extratropical cyclones, which is more similar to subtropical cyclones (cold core and shallow convection at the mature stage). Consequently, they are subjected to baroclinic forcing like extratropical cyclones (Fita et al., 2006; Chaboureau et al., 2012). As such, it is expected that the formation of medicanes is not different from other intense Mediterranean cyclones (Flauonas et al., 2015), and it should be noted that there is no physical criterion to quantify a Mediterranean cyclone into a tropical-like system.

The mechanism of medicane development has been investigated in previous studies. A cut-off low and a potential vorticity anomaly are pre-conditioning factors for medicane initiation (e.g., Miglietta et al., 2016). This triggers deep cumulus convection resulting in the formation of a deep warm core and consequently, a tropical transition of the initial perturbation occurs (Mazza et al., 2017; Fita and Flaounas, 2018). While Miglietta and Rotunno (2019) showed the importance of air-

124   sea interactions for one medicane out of the two studied, they also suggested that the other case

125   medicane is maintained mainly by mid-latitude baroclinic environment (air-sea fluxes and latent

126   heat flux still help to develop the medicane). This aspect is also suggested by Carrió et al. (2017).

127   These discrepancies on the importance of air-sea interaction in the literature may arise from the

128   dependency of the various works on individual case studies. In particular, the importance of air-sea

129   fluxes can be related to wind-induced surface heat exchange (WISHE) mechanism similar to

130   tropical cyclones (e.g., Emanuel, 1986; Miglietta and Rotunno, 2019).

131   In some cases, medicane development involves tropical transition and diabatic heating due

132   to condensation. Understanding the response of such medicane features to anthropogenic global

133   climate change is important for mitigating future risks associated with natural hazards. According to

134   Shaltout and Omdtedt (2014), the Mediterranean SST is expected to increase by 2.6°C per century.

135   This warming in the ocean can be a potential source of enhanced moisture to the atmosphere. In

136   fact, significant changes in medicanes e.g., frequency and intensity associated with global warming

137   have been reported in previous studies. Cavicchia (2014) showed that whereas the frequency of

138   medicanes tends to decrease, medicanes can moderately intensify based on a climate projection

139   with a global coupled model. Tous et al. (2016) also suggested similar future changes in frequency

140   and intensity of medicanes. Their study also revealed that the location of medicane formation is

141   expected to change (more frequent over the Gulf of Lion-Genova and South of Sicily). González-

142   Alemán et al. (2019) concluded that associated with medicane intensification, the structure of

143   tropical-like cyclones is more robust and their lifetime as tropical-like cyclones is longer-lasting

144   compared to medicanes under current climate This, consequently, leads to more hazardous

145   situations in the projected future.

146   Most of the aforementioned studies on the future climate of medicanes are based on results

147   obtained from global coupled models (CGCMs). However, in long climatic simulations performed

148   with CGCMs, the typical grid spacing varies between 100km and 25km, at best. Even simulations

149   at 25km have still an insufficient resolution to resolve the fine-scale structure of medicanes such as

150   the cyclone core and the associated rain bands; the intensity of medicanes is underestimated in most

151   coupled regional models (Gaertner et al. 2018). Therefore, it is most likely that CGCMs also

152   underestimate future changes in medicanes. One possible solution to this problem is to dynamically

153   downscale the global models with a regional climate model (RCM) at finer resolutions (e.g.,

154   Cavicchia and von Storch, 2012; Cavicchia et al., 2014). Alternatively, a pseudo global warming

155   method (PGW, e.g., Schär et al., 1996; Rasmussen et al., 2011; Parker et al., 2018; Mooney et al., in

156   review) can be used to assess more explicitly the impacts of future climate change on medicanes.

157   PGW is an advantageous method to characterise a given medicane in current and future climate by

158   imposing the future changes in atmospheric and ocean variables estimated by CGCMs to boundary

159 conditions of a high-resolution RCM (see details in Section 2). This approach permits a more direct
160 assessment of impacts of future climate change on an extreme weather event (e.g., Parker et al.,
161 2018). Additionally, the PGW method enables investigations of the relative roles of a warmer
162 atmosphere and a warmer ocean in the response of medicanes to climate change.

163 In this study, we use a PGW framework to investigate the impacts of global warming on the
164 development and intensity of medicane Rolf (Miglietta et al., 2013; Ricchi et al., 2017; Dafis et al.,
165 2018). Rolf occurred from 6th to 9th November in 2011 and affected the Balearic Islands, Italy and
166 southern France due to longer persistence of tropical-cyclonic features. Since Rolf was a highly
167 destructive medicane for coastal communities in many Mediterranean countries and is one of the
168 most intense medicanes (e.g., Dafis et al., 2018), it is important to assess how these types of
169 medicanes will respond to climate change in near future. Medicane Rolf generated the deep
170 cumulus convection and persisted with tropical cyclone-like characteristics longer than other
171 Mediterranean storms and vortices (e.g., Miglietta et al., 2013). Moreover, according to Miglietta et
172 al. (2013), Rolf occurred around the Balearic Islands, which is a hot spot of medicane genesis.
173 Therefore, it will be interesting and important to investigate the impacts of climate change on this
174 type of Mediterranean storm. We perform additional idealised experiments in which only the
175 atmosphere or the ocean, respectively, experience global warming to elucidate the roles of a warmer
176 atmosphere and a warmer ocean on the medicane. This study is structured as follows. In Section 2,
177 details of the reanalysis data, RCM and experimental designs are provided. An evaluation and
178 assessment of the simulation of medicane Rolf under current climate conditions with respect to a
179 state-of-the-art reanalysis is presented in Section 3. The results of the PGW experiments are given
180 in Section 4. Additionally, we analyse the possible future changes of the medicane. A more
181 insightful discussion on the competing roles of a warmer atmosphere and ocean in the medicane is
182 examined in Section 5. Finally, the concluding remarks of this study is provided in Section 6.

183

184 **2. Data, Model, and Methodology**

185 In this study, ERA5 reanalysis data (Copernicus Climate Change Service, 2017) is used to
186 benchmark the simulation of medicane Rolf. ERA5 is a state-of-the-art reanalysis system with a
187 high spatio-temporal resolution ($0.25° \times 0.25°$ and 1 hourly). The trajectory of Rolf was estimated
188 from ERA5 by identifying the location of the minimum SLP value at 3-hourly intervals. This track
189 is regarded as the reference track in this study (see Fig. S1). Additionally, we use observational data
190 of the cyclone track produced by the US National Oceanic and Atmospheric Administration
191 (NOAA) using the Dvorak Technique (see Fig. S1). This data is available only from 12UTC, 7 to
192 12UTC,   9   of   November   in   2011
193 (https://www.ssd.noaa.gov/PS/TROP/DATA/2011/tdata/med/01M.html).

194

2.1 WRF Simulation of Rolf under present climate

Rolf is simulated with the Weather Research and Forecasting (WRF, Skamarock et al., 2008) model version 3.9.1. The experimental domains consist of two nested domains as shown in Fig.1: the outer domain has a grid spacing of 15km and the inner domain has a grid spacing of 5km. Both domains have 52 vertical layers. In both domains, a cumulus convection scheme is switched on. Previous studies (e.g., Miglietta et al., 2015; Ricchi et al., 2017; Mooney et al., 2018) have shown that simulated medicanes and tropical cyclones are highly sensitive to different combinations of physical schemes. First, we assessed the convective schemes for better cyclone track among (Kain-Fritsch (Kain 2004), Betts-Miller-Janjíc (Janjíc, 1994), Tiedtke (Tiedtke, 1989; Zhang et al., 2011) in single WRF domain with 10km grid spacing forced by ERA-Interim (Dee et al., 2011) reanalysis data (0.75°×0.75°, 6 hourly). Each simulation has different combinations of microphysics, (WSM5 (Hong et al., 2004), WSM6 (Hong and Lim, 2006), Thompson (Thompson et al., 2008)) and planetary boundary layer (PBL) (Yonsei University (Hong et al., 2006), Mellor-Yamada-Janjíc (MYJ, Janjíc, 1994), Mellor-Yamada-Nakanishi-Niino (MYNN; Nakaish and Niino, 2006; Nakanishi and Niino, 2009; Olson et al., 2019)). According to this assessment simulation, most of simulations with the Tiedtke scheme tend to produce more realistic medicane tracks, making landfall over southern France while simulations with other two convection schemes fail to make a landfall over southern France, make an incorrect landfall over the Sardinia Island or decay over the Mediterranean Sea without landfall (not shown). Based on the results of this assessment, we perform WRF simulation with 6 different combinations of physical schemes; cumulus convection is Tiedke, microphysics scheme is WSM6, WSM5, and Thompson, and PBL scheme is MYNN and MYJ. In Table 2, the combinations of schemes and abbreviation of each combination are given. Since any simulation of tropical cyclones contains a huge uncertainty in its intensity and development (e.g., Torn, 2016), such ensemble simulation will provide more robustness to the expecting results. All simulations use the longwave and shortwave radiative schemes of the Rapid Radiative Transfer Model (Mlawer et al., 1997) and NOAH 4-layer land surface model (Chen and Dudhia, 2001a, b). Initialization and lateral boundary conditions are taken from ERA-Interim 6-hourly reanalysis data (0.75°×0.75°). The lower boundary condition of sea surface temperature (SST) is obtained from daily OISST data with 0.25°×0.25° horizontal resolution. The simulations are integrated from 0000UTC on 05-Nov-2011 to 0000UTC on 10-Nov-2011. Hereafter, these simulations are referred to as PRS, which stands for present-day climate condition. ERA-Interim is selected as the driving data for our WRF simulations to maintain consistency between the spatial resolutions of the PGW delta calculated from the CMIP5 ensemble and the reanalysis data used for the initial and boundary conditions (in particular for atmospheric variables). We also investigated

229   the representation of the medicane Rolf in ERA-Interim and found a cyclone track similar to ERA5

230   (see Section 3 and Fig. S1 for details).

231

232   *2.2 WRF simulation of Rolf under warmer climate*

233   To investigate how future global climate change influences the medicane, a pseudo global

234   warming (PGW, e.g., Parker et al., 2018; Mooney et al., in review) experiment is employed. In the

235   PGW framework, boundary conditions of WRF are perturbed by the monthly-mean values of global

236   climate change (Δ). This is estimated by simulations of climate projections from CGCMs. In other

237   words, we can simulate the medicane Rolf under a virtually warmed climate. In this study, we

238   obtain the PGW Δ from the ensemble mean (see Table 1) of 19 simulations used in the Coupled

239   Model Inter-comparison Project 5 (CMIP5, Taylor et al., 2012) between 2036-2065 and 1976-2005.

240   These periods were chosen on the basis of data availability for CMIP5 CGCMs and to represent

241   1.5°C of global warming in the middle of this century. The advantage of using an ensemble mean of

242   19 GCM realizations over a single GCM realization is that it minimises the influence of unforced

243   natural climate variations and model-errors in quantifying the forced climate response to future

244   GHG warming (Changhai et al., 2017) The PGW Δ contains perturbed values for zonal and

245   meridional winds, temperature, relative humidity, geo-potential, SLP, SST, and skin temperature.

246   The new boundary conditions including the global warming can be expressed as,

247

248    $$BC_{PGW} = BC_{PRS} + \Delta \quad (1),$$

249   where BC_{PGW} represents future boundary conditions and BC_{PRS} represents present day boundary

250   condition from ERA-Interim. Both BC_{PGW} and BC_{PRS} are 6-hourly values, while Δ is a monthly

251   mean value for November. Δ is the PGW perturbation and is defined as follows:

252    $$\Delta = CMIP5_{2036-2065} - CMIP5_{2005-1976} \quad (2),$$

253   These equations are applied to each of the following variables: zonal and meridional winds (U and

254   V), temperature (T), relative humidity (RH), geo-potential (z), SLP, SST, and skin temperature

255   (TSK). In the PGW experiments, we perform three different simulations where the perturbation Δ is

256   added to: (1) all variables at the boundary conditions (PGW_{ALL}), (2) only SST and skin temperature

257   (PGW_{SST}), and (3) only the atmospheric variables (PGW_{ATMS}). This enables an investigation of the

258   relative roles of projected future changes in the atmosphere and ocean in the development and

259   modification of the medicane. Other experimental configurations of PGWs are the same as those in

260   PRS (see section 2.1). Figures 2b and c provide the PGW Δ for SSTs and a vertical profile of

261   atmospheric temperature and relative humidity (averaged over the 5km-mesh domain in Fig. 1) for

262   the PGW experiments in this study. In the Mediterranean Sea, the SST increases approximately by

2°C in Fig. 2b (also shown by Somot et al., 2006). The troposphere is warming by 2 to 3°C in Fig. 2c. In contrast, projections of the relative humidity in the troposphere tend to be reduced under global warming. These projected thermodynamical response to global warming can lead the Mediterranean climate to be warmer and drier (e.g., Giorgi and Lionello, 2008). To the best of our knowledge, the present study is the first investigation to employ the PGW method to a tropical-like cyclone in the Mediterranean Sea.

2.3 Estimation of the Cyclone Phase Space (CPS)

For a trajectory of observed and simulated medicanes, the minimum SLP is tracked from 00UTC-06-Nov-2011 until 12UTC-09-Nov-2011. If the medicane makes a landfall before 12UTC-09-Nov-2011, the tracking is ceased. While not all Mediterranean storms with a warm core undergo a tropical transition (e.g., Fita and Flaounas, 2018), one remarkable characteristic of many medicanes is the cyclonic system transitions from extratropical to tropical (e.g., Gaertner et al., 2018). Hart (2003) proposes an objective measurement of cyclone phase space defined as,

$$\left.\frac{\partial(\Delta Z)}{\partial \ln p}\right|_{900\text{hPa}}^{600\text{hPa}} = -\left|V_T^L\right| \quad (2) \quad \text{and} \quad \left.\frac{\partial(\Delta Z)}{\partial \ln p}\right|_{600\text{hPa}}^{300\text{hPa}} = -\left|V_T^U\right| \quad (3)$$

where,

$$\Delta Z = Z_{\max} - Z_{\min} \quad (4).$$

$Z_{\max}$ and $Z_{\min}$ denote the maximum and minimum geopotential height at a pressure level within 2.5° (for ERA5) and 250km (for WRF simulations) radius around the medicane centre. The upper- and lower- tropospheric thermal wind relation is estimated by equations (2) and (3), respectively. As shown by Hart (2003), in the extratropical phase, the cyclone has a deep cold core and the values of (2) and (3) are negative. In addition, the tropical cyclone has a deep warm core with positive values for (2) and (3). In this study, the thermal wind relation is estimated every 50 hPa from 900 to 300 hPa and the cyclone phase indices of (2) and (3) are defined as mean of the values every 50 hPa between 600 and 300 hP and between 600 and 900 hPa.

3. Simulation of Medicane Rolf under present climate

In this section we examine the results of PRS to assess the ability of our WRF setup to simulate Rolf. The cyclone track of PRS is given in Fig. 3a. In the PRS ensemble simulation, the medicanes have very similar tracks from 00UTC on 6-Nov to 00UTC on 9-Nov shown in Fig. 3a even though there is a spread in the track: firstly, the medicane moves southward and crosses

around the Ibiza Island. After that, it turns northward and finally makes landfall around southern France. This cyclone track reproduces well the observed track (Fig. S1a). The phase shift of the cyclone of PRS ensemble is shown in Figure 3b by cyclone phase space defined by Hart (2003) (see the details of definition in section 2.3). In the beginning, the cyclones of all ensemble members already develop with a shallow warm core (Fig. 3b). This shallow warm core develops into deep warm core at 00UTC on 7-Nov (that is earlier than ERA5 in Fig. S1b). At 00-08-Nov, the simulated cyclone forms a completely deep structure of a warm core. After that, the structure of the deep warm core gradually weakens in all ensemble members. This shift of cyclone phase is approximately consistent with that from ERA5. Thus, PRS can reproduce Rolf in a way that cyclone phase match accordingly the one by ERA5 (Figs. 3 and S1).

Along this cyclone track, a time sequence of SLP of the ensemble-mean cyclone centre is given in Fig. 4. The SLP drops down to 992 hPa at 0600UTC on 06-Nov during the preconditioning period of the tropical-like cyclone. Similar to ERA5 (see Fig. S1c), the SLP of the cyclone increases to 996 hPa until 0000UTC on 07-Nov, decreases again, and consequently the deepening of the low pressure reaches 992 to 993 hPa between 0000 and 0300UTC on 08-Nov (Fig. 4). After this peak, the SLP of the ensemble-mean cyclone increases rapidly approaching southern France (the depression is weakened to 1006 hPa after 22UTC on 08-Nov). The development of the cyclone can be partially linked with the water vapour gained by the cyclone as shown in Fig. 4. The latent heat flux gained by the cyclone increases from the beginning until 06-07-Nov (from 160 to 280 Wm^{-2}) even though this is stronger than in ERA5 (Fig. S1). After this peak, the latent heat flux begins to reduce and is slightly enhanced at 00-08-Nov. The latent heat flux drops again until the landfall over southern France. Surface flux and the corresponding diabatic heating is an energy source of transition from extratropical to subtropical and tropical-like cyclones (e.g., Emanuel, 2005; Quitián-Hernández et al., 2020). Rolf also obtains a huge amount of water vapour from the underlying sea surface during its phase transition and development. The maximum value of latent heat flux reaches 740W/m^2 in one grid box at the cyclone peak, while this value is less than two cases of Mediterranean storms (Miglietta and Rotunno, 2018). In that study, the two Mediterranean storms were closer to the African Continent than the Rolf and therefore, dry air from the African Continent and warmer SST would enhance the evaporation more effectively than our case. In the PRS simulations, the precipitation associated with the cyclone is intense at 0000UTC on 06-Nov and decreases until 1200UTC on 06-Nov in Fig. 4. That can be associated with deep cumulus convection due to the initial disturbance (not shown). After 1200UTC on 06-Nov, the precipitation remains in a relatively small amount with some fluctuations before increasing again at 1200UTC on 07-Nov reaching a peak around 20 to 2100UTC on 07-Nov, which is somewhat earlier than the peak of SLP depression. Coinciding with the reduction in the SLP depression, the precipitation

decreases again after the peak. The red contour shows an averaged wind speed exceeding the 95th percentile (referred to as maximum wind speed, MWS, hereafter) around the cyclone in each simulation. The MWS is defined as an averaged value of 10m-wind speed at a grid box where the wind speed exceeds 95th percentile every hour within 250km radius of the cyclone. In PRS, from 0000UTC on 06-Nov until 1200UTC on 07-Nov, the MWS does not show a clear variation (18m/s to 21m/s) and after that, increases until 0800UTC on 08-Nov, reaching to 24m/s. This variation is roughly consistent with that in the SLP (Fig. 4) even though the timing is relatively delayed in the MWR compared to SLP.

The difference in intensity and transition timing between ERA5 and PRS may be caused by the difference in evaporation and condensation the cyclone gains. However, PRS is able to realistically reproduce the medicane Rolf and the impact of climate change on Rolf will be described in the next section.

4. Simulation of Medicane Rolf under 1.5°C global warming

As explained in Section 2, we explore how Rolf is affected by the future climate change (middle of the 21st century), which corresponds to global warming of 1.5°C using the pseudo global warming (PGW: e.g., Schär et al., 1996; Rasmussen et al., 2011; Parker et al., 2018) technique. In addition to the effects of climate change, the relative roles of the atmosphere and the ocean in the modulations of medicane Rolf are also investigated separately in this section.

Figure 5 shows the simulated cyclone tracks of Rolf in the PGW experiments for a 6-member multi-physical ensemble. PGW$_{ALL}$ reproduces a very similar cyclone track to that in PRS (Fig. 3a). From the beginning, the cyclone moves southward approaching the Balearic Islands. After that, the cyclone progresses northward and makes landfall over southern France. While this behaviour is not considerably different from that in PRS, a few other differences can be detected. Under the future climate change, no simulated Rolfs makes landfall over Ibiza while some of PRS medicanes hit Ibiza (Fig. 3a). This indicates that the latitude where the cyclone shifts its direction from south to north tends to be relatively higher than that in PRS (Figs. 3a and 5a). Some of ensemble cyclones make landfall slightly earlier than PRS. These modifications in the cyclone track are more remarkable in PGW$_{SST}$ shown in Fig. 5b. The simulated medicanes change their marching direction to the north at a much higher latitude (higher than 40°N) in all ensemble members, far from the Balearic Islands, at 0000UTC on 07-Nov. After this shift, the cyclone moves northward similar to PRS and PGW$_{ALL}$, but its direction shifts more westward than PRS and PGW$_{ALL}$. Due to those modifications, the simulated medicanes make landfall (one medicane of TD_TP_MJ disappears over the Mediterranean Sea) over southern France at 3.8°E, which is more western than PRS and PGW$_{ALL}$, and the landfall is much earlier than PRS and PGW$_{ALL}$, which is at 1200UTC to

1800UTC on 08-Nov. Interestingly the PGW_ATMS simulations of Rolf show a clearly opposite tendency of changes to PGW_ALL and PGW_SST in Fig. 5c. Many of simulated cyclones strike Ibiza like PRS, but the cyclones in PGW_ATMS progresses more southward while the cyclone in PRS moves eastward after this landfall on Ibiza (Figs. 5c). The cyclones in PGW_ATMS still moves eastward after 0000UTC on 07-Nov and finally change its direction to north around 1200UTC on 07-Nov, which is later by 6 and 12 hours than PRS or PGW_ALL and PGW_SST. Instead of moving westward, the cyclone in PGW_ATMS orientates to the northeast and approaches southern France around 7°E at 0000UTC on 09-Nov shown in Fig. 5c. The response of the cyclone tracks to climate change seems different between PGW_ALL/PGW_SST and PGW_ATMS and we see how the other features of the cyclone will change in the PGW experiments.

Figure 6a gives a time series of ensemble-mean SLP in the cyclone centre of PGWs along the cyclone tracks in Figs. 5. Rolf in PGW_ALL develops the SLP centre in quite a similar way to Rolf in PRS. In the beginning, the SLP depresses once to 991 hPa at 0700UTC on 06-Nov and increases the SLP of the centre until 0000UTC on 07-Nov. Again, the SLP reduces and reaches the other minimum of 991hPa at 2200 on 07-Nov to 0000UTC on 08-Nov. This SLP depression is slightly lower in PGW_ALL than in PRS. While the difference of SLP depression between PRS and PGW_ALL is small, the SLP gradient around the centre is different. Figure 7 shows the scalar of SLP gradient for PRS and PGW_ALL at the maximum of SLP depression. It is obvious that the SLP gradient is much stronger in the PGW_ALL than in the PRS around the peak time (PRS is 0.0004 hPa/m and PGW_ALL is 0.0007 hPa/m) indicating that the warmer climate induces the stronger wind in the centre, which could be linked to changes in precipitation (this aspects is later described). Compared to PRS, the cyclone in PGW_ALL decays relatively rapidly after the peak at 0600UTC on 08-Nov, in particular, after 1200UTC on 08-Nov. This is likely to be due to the earlier time of landfall of some of the PGW_ALL cyclones over southern France (Figs. 3b and Fig. 5a). Inversely, the SLP of the PGW_SST cyclone drops down intensively to 987 hPa from 0000UTC to 1000UTC on 06-Nov. The SLP centre in the PGW_SST generally continues to decrease until 2100UTC on 07-Nov reaching 982 hPa. This is a slightly earlier peak time and much lower SLP in the cyclone centre than those in PRS and PGW_ALL. After this peak, the cyclone in the PGW_SST decays quite rapidly (approximately 20 hPa per 24 hours between 2100UTC on 7-Nov and 2100UTC on 08-Nov). This is associated with the earlier landfall time compared to PRS and PGW_ALL (Figs. 3b, 5a and 5b). It is noteworthy that in the PGW_ATMS, the SLP generally increases throughout cyclone tracking. While initially, the ensemble-mean SLP of the PGW_ATMS cyclone centre is almost identical to those of PRS and PGW_ALL, the second depression of the cyclone centre after 0000UTC on 07-Nov is much weaker than PRS and PGW_ALL. The second reduction in SLP is detected at 2100UTC on 07-Nov (slightly earlier than PRS), but it reduces only to 997 hPa. The cyclone begins to decay gradually

11

after this. Interestingly, this result suggests that the role of future climate change in the atmospheric and oceanic background have competing effects on the medicane development.

Figure 6b shows a time series of latent heat flux gained (averaged) by the simulated cyclone within a radius of 250 km. The evaporation in PGW_{ALL} is marginally larger than that in PRS, especially from the beginning at 0000UTC on 06-Nov to 1200UTC on 07-Nov (approximately 50 W/m^2 higher at largest). During this period, the temporal variation in evaporation along the cyclone track is almost identical between PRS and PGW_{ALL}. In PGW_{SST}, the simulated cyclones obtain much more water vapour from the underlying warmer SST. Initially, the latent heat flux is about 1.5 times more in PGW_{SST} than that in PRS and increases up to 450 W/m^2 until 1200UTC on 07-Nov. The uptake of water vapour drops suddenly after 2000UTC on 07-Nov and becomes lesser than that in PRS at 0700UTC on 08-Nov and is diminished to a few tens of W/m^2 after the earlier landfall. Inversely, the evaporation in PGW_{ATMS} is less than that in PRS during the entire period of cyclone tracking. However, the temporal variation in evaporation is quite similar to that in PRS having a peak between 00UTC to 0600UTC on 07-Nov. The decreasing rate of the evaporation after the peak in PGW_{ATMS} is relatively more moderate than those in PGW_{ALL} and PGW_{SST} probably due to the later time of the landfall (Fig. 5c). While the uptake of water vapour differs among PGWs, its peak leads the maximum of the medicane similarly by 6 to 12 hours (Figs. 6a and 6b).

The precipitation in PGW_{ALL} shows quite a similar variation to that in PRS until 0900UTC on 07-Nov (see Fig. 6c) although the precipitation is slightly stronger. While the precipitation in PGW_{ALL} increases at almost the same time as PRS, its maximum value around 1900UTC on 07-Nov is larger than that in PRS (PGW_{ALL} is 1.8mm/h and PRS is 1.4mm/h). This implies that the simulated cyclone in PGW_{ALL} can obtain more energy from diabatic heating than PRS, which could result in a stronger SLP gradient shown in Fig. 7. This stronger precipitation can be associated with an enhanced uptake of the water vapour in PGW_{ALL} as shown in Fig. 6b. In PGW_{SST}, the precipitation is very similar to that in PRS and PGW_{ALL} at the beginning. However the precipitation keeps its relatively strong intensity and consequently, the difference from PGW_{ALL} and PRS is large during the cyclone lifetime. After 0000UTC on 07-Nov, precipitation increases and its peak increases and peaks at 2.6 mm/hour before 2100UTC on 07-Nov. This value is 31.2mm/12h of PGW_{SST} (within 250km radius) that can be classified to the extremely intense precipitation event in the Mediterranean Sea according to Fig. 8 of Flaounas et al. (2019). The precipitation of PRS (approximately 18mm/12h) can still be classified as an intense rainfall event in the Mediterranean Sea by Fig. 8 of Flaounas et al. (2019). After this, the precipitation is abruptly reduced due to the earlier timing of the landfall (Fig. 5b). This intense rainfall can be associated with the increased water vapour available in PGW_{SST} (Fig. 6b). The precipitation of PGW_{ATMS} also shows an identical variation with PRS in the beginning of the track. Associated with the moderate latent heat flux in

Fig. 6b, the precipitation is less during the whole lifecycle of the cyclone and does not show a clear peak (two small peaks at 1700UTC on 07-Nov and 0600UTC on 08-Nov) with a smaller amount than those in PRS and other PGWs.

Figure 6d illustrates a time series of MWS for the PGW experiments. In PGW$_{ALL}$, the hourly changes in MSW are similar to those in PRS, but that is stronger than in PRS through most of its lifecycle (at largest, 6m/s higher in PGW$_{ALL}$). The maximum value of MWS reaches 26m/s at 0000UTC on 8-Nov. After 0600UTC on 08-Nov, the MWS in PGW$_{ALL}$ gradually reduces and eventually its value becomes smaller than that of PRS. This could be caused by the slightly earlier landfall in PGW$_{ALL}$ than PRS (Fig. 5a). In PGW$_{SST}$, the MWS is almost identical to that in PGW$_{ALL}$ until 0000UTC on 7-Nov. After this time, the MWS in PGW$_{SST}$ gets stronger than that in PGW$_{ALL}$ and an increase rate of in MWS is about 8 m/s between 1200UTC on 7-Nov and 0000UTC on 8-Nov reaching 30 m/s at 0000UTC on 8-Nov. The MWS falls down rapidly (from 28m/s to 12 m/s per 14 hours) after 0500UTC on 8-Nov probably due to the earlier landfall (Fig. 5b). In PGW$_{ATMS}$, during 06 and 07-Nov, the MWS is stronger than that in PRS. However, after 0000UTC on 08-Nov, the MWS in PGW$_{ATMS}$ is weaker than that in PRS resulting in a smaller maximum amplitude of MWS during the cyclone tracking in PGW$_{ATMS}$ is smaller than in PRS (21m/s for PGW$_{ATMS}$ and 24m/s for PRS). In addition, as seen in Fig. S2, the ratio of grid boxes with weaker wind speeds (category of 5 to 10m/s) is larger in PGW$_{ATMS}$ than in PRS (in particular, 12UTC-07 and 08UTC-08). That is, the area of strong winds is much smaller in PGW$_{ATMS}$ than in PRS (the horizontal distribution of winds will be given in Fig. 9).

Figure 8 illustrates a diagram of the cyclone phase space in PGWs. Whilst the phase shift from a shallow to a deep warm core is almost identical in the PRS and PGW$_{ALL}$, the warm core of PGW$_{ALL}$ simulated cyclone is relatively stronger, especially, in the lower troposphere (Fig. 8a). Towards the end of tracks, the structure of the deep warm core in some members of the PGW$_{ALL}$ (TD_W6_MN and TD_TP_MJ) are diminished substantially in and this is due to the earlier landfall than PRS. In PGW$_{SST}$, the simulated cyclones change their phase from shallow to deep warm core in a similar way to PRS and PGW$_{ALL}$ (Fig. 8b). However, once the cyclone shifts to a deep warm core, the structure of the deep warm core is strengthened and consequently, some ensembles of simulated cyclones reach much larger values of deep warm core (the values in both troposphere reach more than 200) than PRS and PGW$_{ALL}$. Due to the much earlier landfall, the structure of the deep warm core of some ensembles members shrinks abruptly after its mature state and eventually the cyclone is reduced to one with a cold core at the end of track. The phase shift of the cyclone in PGW$_{ATMS}$ is also similar to those in PRS and PGW$_{ALL}$ in Fig. 8c. In contrast, after the cyclone is converted into a tropical-like cyclone from, the development of a deep warm core is not as strong as PRS and other PGWs. The maximum value of the deep warm core phase is smaller than those of

471 PRS and other PGWs (in both troposphere, it is around 100). There is no rapid reduction of warm

472 core in PGW_{ATMS} since the cyclone achieves the landfall later than other PGWs Fig. 5c.

473   Under global warming, the development of the medicane is modified with respect to that of

474 the present day (in particular, a moderate intensification as aforementioned from Figs. 6 to 8). Here,

475 we explore the horizontal structure of the medicane. The wind speed of PRS exceeds 24 m/s at the

476 peak of SLP depression (based on Fig. 5a) in Fig. 9a. Within 100km radius, the wind speeds are 20

477 m/s. In PGW_{ALL}, while the radius of high wind speeds appears to be slightly smaller, the wind

478 speed is 24 m/s over a large part within the radius of 100km (see Fig. 9b) and the maximum values

479 (faster than 26 m/s) is larger than that of PRS. This result is consistent with the stronger SLP

480 gradient around the cyclone centre in PGW_{ALL} as shown in Fig. 7. Regarding the intensification in

481 the SLP depression, the surface wind speed is much stronger in PGW_{SST} than PRS and PGW_{ALL} in

482 Fig. 9c. The wind speed exceeds 30 m/s in the most areas within the radius of 100km (except for the

483 centre). In contrast, wind speeds for the cyclone in PGW_{ATMS} are substantially lower. Its maximum

484 of wind speed is 22 to 24 m/s, which is equivalent to that in PRS (as shown Fig. 7d, the hourly

485 MWS in PGW_{ATMS} is larger than that in PRS), but the area of high speed winds is obviously

486 diminished in Fig. 9d and the strong wind speed is limited only in the northern sector around the

487 centre. This result is consistent with Fig. S2.

488   Figure 10 illustrates the rainband structure of each simulated cyclone during the

489 precipitation peak given in Fig. 6c. In PRS, the cyclone has a spiral band of precipitation around the

490 centre (Fig. 10a). In particular, the precipitation is active (up to 9-10 mm/h) in the northern sector of

491 the cyclone and the strong rainfall extends to the northeast direction within a radius of 150 km.

492 There is little rainfall in the centre area, which could be cloud-free "eye"; this can be easily

493 detected, and it is also a key feature of tropical-like cyclones. As seen in Fig. 6c the precipitation of

494 PGW_{ALL} intensifies during its peak in Fig. 10b. Whereas the spiral band of precipitation is likely to

495 be similar to that in PRS in the northern sector, the precipitation is intense than PRS around the

496 centre (reaches 16mm/h) and the southern sector. It seems that the spiral rainband of the medicane

497 is reinforced due to projected global warming. The eye of the medicane is larger than that in PRS.

498 The warmer SST enhances the spiral band more effectively in Fig. 10c as shown in Fig. 6c. The

499 precipitation around the centre exceeds 16 mm/h in the southern sector and the northeastward

500 rainband is elongated with intense rainfall. In the far side of the southern sector, the rainband is

501 more activated (up to 8 mm/h) compared to PGW_{ALL}. This is associated with the much deeper

502 depression of SLP and stronger wind in PGW_{SST} (Figs. 5a and 9c). Corresponding to the

503 deactivated precipitation due only to the warmer atmosphere (Fig. 7c), the rainband around the

504 cyclone centre in PGW_{ATMS} is reduced significantly as shown in Fig. 10d. While the maximum

505 rainfall is still more than 14 mm/h near the centre, the rainband almost loses its spiral structure and

506 the area of intense rainfall is limited only around the cyclone centre.

507

5. Discussion on relative role of warmer atmosphere and ocean in medicane development

509 In the previous section we showed that the warmer climate leads to a moderate medicane

510 intensification in agreement with previous studies (e.g., Cavicchia et al., 2014; Tous et al., 2016;

511 González-Alemán et al., 2019). The results also showed more enhanced precipitation, surface wind

512 speed and a SLP deepening around the medicane. Interestingly though, the warmer atmosphere

513 inhibits the medicane development substantially, while the warmer ocean enhances the medicane

514 considerably. In this section, we discuss the roles of the atmosphere and the ocean in the

515 medicane's response to future warming.

516 Figure 11a gives a time function of convective available potential energy (CAPE) averaged

517 within the 250km radius around the cyclone centre. CAPE in PRS increases from the beginning and

518 reaches its peak (400 Jkg^{-1}) around 1000UTC on 07-Nov. This peak occurs earlier than the

519 maximum of precipitation as shown in Fig. 6c. In the remaining time, CAPE decreases

520 corresponding to the decay of the cyclone. PGW_{ALL} has a slightly larger CAPE than PRS. CAPE

521 becomes smaller in PGW_{ALL} than PRS after the peak probably because the cyclones in PGW_{ALL}

522 tend to make a slightly earlier landfall. Such a difference is most obvious in PGW_{SST}. CAPE in

523 PGW_{SST} becomes much larger at 1200UTC on 06-Nov (250 Jkg^{-1}) and the timing of its peaks is at

524 0700UTC on 7-Nov, which is relatively earlier than PRS. After the peak, CAPE decreases much

525 more abruptly than PGW_{ALL} partially due to the earliest time of landfall. Inversely, CAPE in

526 PGW_{ATMS} is smaller than PRS during the almost entire cyclone track. Figures 11b-e give CAPE of

527 each WRF simulation at its maximum in Fig. 11a. Between PRS and PGW_{ALL}, the simulated

528 cyclones gain more energy in PGW_{ALL} (at maximum, 800 J kg^{-1} for PRS and more than 1000 Jkg^{-1}

529 for PGW_{ALL}, Figs. 11b and 11c) resulting in the enhanced precipitation. In PGW_{SST}, the simulated

530 medicanes also obtain a lot of energy like PGW_{ALL} and the area of large CAPE (more than 1000 J

531 kg^{-1}) spreads more widely around the cyclone centre than PRS and PGW_{ALL} (Fig. 11d). In addition,

532 the CAPE is larger in the northen sector of the PGW_{SST} medicane than other simulated medicanes

533 (800 to 900 J kg^{-1}). This wider area of high CAPE is consistent with the larger area of intense

534 precipitation (Fig. 10c). Contrastingly, CAPE in PGW_{ATMS} shrinks extensively and its size of high

535 CAPE is much smaller than PRS.

536 Figure 12 gives the outgoing longwave radiation (OLR) as a proxy of cumulus convection

537 during the time of maximum rainfall (see Fig. 6c) in each experiment. In PRS, the deep cumulus

538 convection is well developed (the OLR is 140-150Wm^{-2}) around the medicane centre during the

539 rainfall peak (Fig. 12a). Inversely, the high OLR (240-260Wm^{-2}) is detected in the centre, which

could be a cloud-free area. In PGW_{ALL}, the low OLR (140-160Wm-2) is extended more to the northern sector of the simulated medicane than PRS (Fig. 12b). The cloud free area in the centre seems to be larger than PRS. Due to the warmer SST, the deep cumulus convection is reinforced indicating by the much lower OLR around the medicane centre in PGW_{SST} (130-140 Wm^{-2}, Fig. 12c). The cloud free area is quite similar to that in PGW_{ALL}. In PGW_{ATMS}, contrastingly, the low OLR area reduces considerably and the southern sector of the medicane is covered with high OLR (240Wm^{-2}). While the cloud free area in the centre has a same size as that of PRS, the OLR is relatively lower than that of PRS (210 Wm^{-2}), indicating that the feature of tropical-like cyclone is weakened in PGW_{ATMS}. These CAPE and OLR differences are consistent well with the results of precipitation differences (Figs. 5c and 10).

In PGW_{SST}, due to the warmer underlying SST, the latent heat flux is activated efficiently and the atmospheric conditions favour cumulus convection. In addition to the evaporation, surface wind associated with the medicane is also substantially enhanced during the cyclone's lifetime (especially before and at the peak). This possibly indicates that the WISHE mechanism is enhanced in PGW_{SST}. Conversely, in PGW_{ATMS}, the background troposphere is warmed and drier through the entire troposphere compared to PRS (Fig. 2c). Even though the ocean forcing is similar in PRS and PGW_{ATMS} (since the SST boundary condition does not differ), the warmer temperature and the lower relative humidity due to global warming (Fig. 2c) is unfavourable for condensation. This means that CAPE is reduced resulting in reduction in deep cumulus convection (Fig. 12d). That is, the diabatic heating is less effectively generated and the WISHE mechanism and the SLP depression are also reduced in PGW_{ATMS}. The moderate intensification of the medicane in PGW_{ALL} is a consequent of the competition between enhancement due to the warmer SST and suppression due to the warmer/drier atmosphere.

However, we need to consider the role of SST change due to surface wind and evaporation. When evaporation is more effective in PGW_{SST} and less effective in PGW_{ATMS}, the underlying SST can be cooled down and warmed up. Due to the regional climate model used in this study, our result do not consider the two-way interactions between the atmosphere and ocean, and how this impacts the response of medicane characteristics in a warmer climate. Future work will investigate these impacts on the medicane with an coupled atmosphere-ocean regional climate model (e.g., Akhtar et al., 2014; Mooney et al., 2016; Ricchi et al., 2019) in the future to increase robustness of our results in this study.

6. Concluding Remarks

In this study we investigated the impacts of future climate change on a tropical-like cyclone (medicane) formed in the Mediterranean Sea in a PGW framework with the WRF regional climate

16

model. The main novelty of this work is the investigation of the relative roles of the atmosphere and ocean, respectively in the medicane's response to projected global warming.

We performed 6 physical ensemble simulations of the medicane Rolf under present (PRS) and future warming conditions of 1.5°C by applying the PGW method for RCP8.5 according to the middle of the 21st century (e.g., Parker et al., 2018; Mooney et al., in review). Compared to the reference track of ERA5 reanalysis, PRS of WRF simulates Rolf realistically making a landfall over southern France. While the SLP depression of Rolf is stronger in PRS than in ERA5 partially because of difference in grid size, the SLP deepening decreases to 992 hPa in PRS, which is consistent well with previous studies (e.g., Miglietta et al., 2013). PRS also represents well the phase transition to a tropical-like cyclone with a deep warm core.

The PGW experiments revealed obvious changes in medicane structure associated with global warming. Firstly, there are clear impacts on the cyclone track: in PGW$_{ALL}$ and PGW$_{SST}$, the medicane tends to move into more northern and western pathway and its timing of landfall becomes earlier than PRS (in particular in PGW$_{SST}$). Conversely, the medicane in PGW$_{ATMS}$ shifts more southward and eastward. This difference in cyclone track might not be a random response, but it seems to be associated with changes in the intensity of the medicane. In PGW$_{ALL}$ and PGW$_{SST}$, the medicane is more enhanced in terms of surface wind and precipitation around the cyclone centre (e.g., Cavicchia et al., 2014; González-Alemán et al., 2019) and the degree of intensification is much stronger in PGW$_{SST}$ and PGW$_{ALL}$ (e.g., the hourly maximum wind speed reaches 30 m/s in PGW$_{SST}$ in Fig. 6d). The cyclone track of the stronger medicane in PGW$_{SST}$ is more to the north and, consequently, makes an earlier landfall than in PGW$_{ALL}$. Inversely, the medicane in PGW$_{ATMS}$ reduces its intensity to a large extent with a smaller size of region with high wind speed. The northward shift in position of the maximum wind speed associated with the medicane is also detected in a climate projection by Tous et al. (2016). The changes in cyclone track shown in this study might be indicative for the results of Tous et al. (2016). However, since our simulations address only one medicane with 6-member multi-physical ensembles, we will need to investigate the changes in cyclone track due to global warming in other case studies, so that the implication for medicanes more generally becomes more robust.

Our PGW simulations elucidated the counteracting individual contributions of a warmer atmosphere and a warmer ocean to the development of medicanes associated with global warming. Since the warmer and drier atmosphere reduces cumulus convection indicated by weaker CAPE and larger OLR, the energy due to diabatic heating is not sufficient. This situation can be ineffective to drive the WISHE mechanism (hourly maximum wind speed is approximately equivalent between PRS and PGW$_{ATMS}$, but the area of high wind speed is much smaller in PGW$_{ATMS}$ than in PRS). Consequently, the transition from a cut-off low into a tropical-like cyclone tends to be degraded.

Conversely, the warmer ocean surface enriches the medicane with moisture, which allows cumulus convection to develop more effectively (Figs 11c and 12c). With a more efficient energy gain, the medicane growth is enhanced and WISHE (e.g., Eamanuel, 1986) can be also activated, as indicated by the results of PGW$_{SST}$. Consolidating these reversal effects of warmer (and drier) atmosphere and ocean (through nonlinear processes), the medicane intensifies to a moderate extent by global warming. While the medicane under global warming shows a modest intensification (e.g., Cavicchia et al., 2014) in terms of wind speed and SLP deepening, precipitation presents radical changes during the peak of intensity. This suggests that the medicane could be more hazardous due to global warming as concluded by González-Alemán et al. (2019).

The PGW technique is a powerful tool to investigate the impacts of climate change on the weather systems in the future. However, our results in this paper include only the climate changes in background such as temperature, relative humidity, SST and etc. In this framework, any changes in extratropical dynamics like wave breaking and large-scale circulation as a source of medicanes are not directly considered. Additionally, as Flaounas et al. (2019) suggest, the water vapor transport from the North Atlantic sector will be modified and significantly influences the medicane frequency and intensity. The PGW approach does not reflect directly such future change in water vapour transport. Nonetheless, we can conclude that the background change associated with global warming will have some impact on the medicane development.

In this study we have presented novel findings regarding the relative roles of atmosphere and ocean in the modulation of medicane development under global warming. It would be interesting to see if other cases of medicanes show a similar response to the warmer atmosphere and ocean. For a better quantification of changes, the simulation and investigation with a regional coupled model for several cases will be desired in the future.

Reference

645

646 Akhtar, N., Brauch, J., Dobler, A., Béranger, K., and Ahrens, B.: Medicanes in an ocean-
647   atmosphere coupled regional climate model. *Nat. Hazards Earth Syst. Sci*., **14**, 2189-2201,
648   doi:10.5194/nhess-14-2189-2014, 2014.

649 Bakkensen, L. A.: Mediterranean Hurricanes and Associated Damages Estimates.
650   *J. Extreme Events*, **4** (2), https://doi.org/10.1142/S2345737617500087, 2017.

651

652 Bouin, M.-N., and Lebeaupin Brossier, C.: Surface processes in the 7 November 2014 medicane
653   from air-sea coupled high resolution numerical modeling. *Atmos. Chem. Phys*., **20**,
654   6861-6881, https:/doi.org/10.5194/acp-20-6861-2020, 2020.

655 Camargo, S., Sobel, A. H., Barnston, A. G., and Emanuel, K. A.: Tropical cyclone genesis
656   potential index in climate models. *Tellus A*, **59**, 428-443, https://doi.org/10.1111/j.1600-
657   0870.2007.00238.x, 2007.

658 Caniaux, G., Giordani, H., Redelsperger, J.-L., Guichard, F., Key, E., and Wade, M.:
659   Coupling between the Atlantic cold tongue and the West African monsoon in boreal spring
660   and summer. J. *Geophys. Res. Oceans*, **116**, C04003, doi:10.1029/2010JC006570, 2011.

661 Cavicchia, L., and von Storch, H.: The simulation of medicanes in a high-resolution regional
662   climate model. *Clim. Dyn*., **39** (9), 2273-2290, https://doi.org/10.1007/s00382-011-1220-0 ,
663   2012.

664 Cavicchia, L., von Storch, H., and Gualdi, S.: A long-term climatology of medicanes.
665   *Clim. Dyn*., **43**, 1183-1195, https://doi.org/10.1007/s00382-013-1893-7, 2013.

666 Cavicchia, L., von Storch, H., and Gualdi, S.: Mediterranean Tropical-Like Cyclones n
667   Present and Future Climate. *J. Climate*, **27**, 7493-7501
668   https://doi.org/10.1175/JCLI-D-14-00339.1, 2014.

669 Chaboureau, J. P., Pantillon, F., Lambert, D., Richard, E., and Claud, C.: Tropical transition
670   of a Mediterranean strom by jet corssing. *Q. J. Roy. Meteorol. Soc*., **138**, 596-611,
671   https://doi.org/10.1002/qj.960, 2012.

672 Copernicus Climate Change Service : ERA5: First generation of ECMWF atmospheric
673   reanalyses of the global climate. Copernicus Climate Change Service Data Store (CDS),
674   *data of access*. http://cds.climate.copernicus.eu/cdsapp#!/home , 2017.

675 Dafis, S., Rysman, J.-F., Claud, C., and Flaounas, E.: Remote sensing of deep convection
676   within a tropical-like cyclone over the Mediterranean Sea. *Atmos. Sci., Lett*., **19**, e823,
677   https://doi.org/10.1002/asl.823, 2018

678 Dee, D. P., Uppala, S. M., Simmons, A. J., Berrisford, P., Poli, P., Kobayashi, S., Andre, U.,
679   Balmaseda, M. A., Balsamo, G., Bauer, P., Bechtold, P., Beljaars, A. C. M., van de Berg, L.,

680   Bidlot, J., Bormann, N., Delsol, C., Dragani, R., Fuentes, M., Geer, A. J., Haimberger, L.,

681   Healy, S. B., Hersbach, H., Hóml, E. V., Isaksen, L., Kåkkberg, P., Köhler, M., Matricardi,

682   M., McNally, A. P., Monge-Sanz, B. M., Morcrette, J.-J., Park, B.-K., Peubey, C., de

683   Rosnay, P., Tavolato, C., Thépaut, J.-N., and Vitart, F.: The ERA-Interim reanalysis:

684   configuration and performance of the data assimilation system. *Q. J. Roy. Meteorol. Soc.*,

685   **137**, 553-597, https://doi.org/10.1002/qj.828, 2011.

686   Emanuel, K. A.: An air-sea interaction theory for tropical cyclones. Part I: Steady-state

687   maintenance. *J. Atmos. Sci.*, **43**, 585-604, 1986.

688   Emanuel, K. A.: Genesis and maintenance of "Mediterranean hurricanes". *Adv. Geosci.*, **2**,

689   217-220, 2005.

690   Fita, L., Romero, R., and Ramis, C.: Intercomparison of intense cyclogenesis events over the

691   Mediterranea basin based on baroclinic and diabatic influence. *Adv. Geoscience*, **7**, 333-342,

692   2006

693   Fita, L., and Flaounas, E.: Medicanes as subtropical cyclones: the December 2005 case from

694   the perspective of surface pressure tendency diagnostic and atmospheric water budget.

695   *Q. J. Roy. Meteorol. Soc.*, **144**, 1028-1044, https://doi.org/10.1002/qj.3273, 2018.

696   Flaounas, E., Fita, L., Lagouvardos, C., and Kotroni, V.: Heavy rainfall in Mediterranean cyclones,

697   PartII: Water budget, precipitation efficiency and remote water sources. *Clim. Dyn.*, **53**,

698   2539-2555, https://doi.org/10.1007/s00382-019-04639-x

699   Gaertner, M. Á., González-Alemán J. J., Romera R., Domínguez M., Gil, V., Sánchez, E., Gallardo,

700   C., Miglietta, M. M., Walsh, K. J. E., Sein, D. V., Somot, S., Dell'Aquila A., Teichmann,

701   C., Ahrens, B., Buonomo, E., Colette, A., Bastin, S., van Meijgaar, E., and Nikulin, G.:

702   Simulation of medicanes over the Mediterranean Sea in a regional climate model

703   ensemble: impact of ocean-atmosphere coupling and increased resolution.

704   *Clim. Dyn.*, **51** (3) 1041-1057, https://doi.org/10.1007/s00382-016-3456-1, 2018.

705   Giorgi, F., and Lionello, P.: Climate change projections for the Mediterranean region.

706   *Glob. Planet. Change*, **63** (2-3), 90-104, doi:10.1016/j.gloplacha.2007.09.005, 2008.

707   González-Alemán, J. J., Pascale, S., Gutierrez-Fernandez, J., Murakami, H., Gaertner, M. A., and

708   Vecchi, G. A.: Potential Increase in Hazard From Mediterranean Huriicane Activity

709   With Global Warming. *Geophys. Res. Lett.*, **46**, 1754-1764,

710   https://doi.org/10.1029/2018GL081253, 2019.

711   Hart, R. E.: A Cyclone Phase Space Derived from Thermal Wind and Thermal Asymmetry.

712   *Mon. Wea. Rev.*, **131**, 585-616, 2003.

713   Hong, S.-Y., Dudhia, J., and Chen, S.-H.: A revised approach to ice microphysical processes

for the bulk parameterization of clouds and precipitation. *Mon. Wea. Rev.*, **132,** 103–120, 2004.

Hong, S.-Y., and Lim, J.–O. J.: The WRF single–moment 6–class microphysics scheme (WSM6). *J. Korean Meteor. Soc.*, **42**, 129–151, 2006.

Hong, S.-Y., Noh, Y., and Dudhia, J.: A new vertical diffusion package with an explicit treatment of entrainment processes. *Mon. Wea. Rev.*, **134**, 2318–2341. doi:10.1175/MWR3199.1 , 2006.

Janjic, Z. I.: The Step–Mountain Eta Coordinate Model: Further developments of the convection, viscous sublayer, and turbulence closure schemes. *Mon. Wea. Rev.*, **122**, 927–945, 1994.

Jin, F.-F.: Tropical Ocean-Atmosphere Interaction, the Pacific Cold Tongue, and the El Niño-Southern Oscillation. *Science*, **274** (5284), 76-78, doi:10.1126/science.274.5284.76, 1996.

Kain, J. S.: The Kain–Fritsch convective parameterization: An update. *J. Appl. Meteor.*, **43**, 170–181, 2004.

Mazza, E., Ulbrich, U., and Klein, R.: The Tropical Transition of the October 1996 Medicane in the Western Mediterranean Sea: A Warm Seclusion Event. *Mon. Wea. Rev.*, **145**, 2575-2595, 2017.

Miglietta, M. M., Laviola, S., Malvaldi, A., Conte, D., Levizzani, V., and Price, C.: Analysis of tropical-like cyclones over the Mediterranean Sea through a combined modeling and satellite approach. *Geophys. Res. Lett.*, **40**, 2400-2405, doi:10.1002/grl.50432, 2013.

Miglietta, M. M., Mastrangelo, D., and Conte, D.: Influence of physics parametrization schemes on the simulation of a tropical-like cyclone in the Mediterranean Sea. *Atmos. Res.*, **153**, 360-375, https://doi.org/10.1016/j.atmosres.2014.09.008, 2015.

Miglietta, M. M., Cerrai, D., Laviola, S., Cattani, E., and Levizzani, V.: Potential vorticity patterns in Mediterranean "huricanes". *Geophys. Res. Lett.*, **44**, 2537-2545, doi:10.1002/2017GL072670, 2017.

Miglietta, M. M., and Rotunno, R.: Development mechanisms for Mediterranean tropical-like cyclones (medicanes). *Q. J. Roy. Meteorol. Soc.*, **145**, 1444-1460, doi:10.1002/qj.3503, 2019

Mlawer, E. J., Taubman, S. J., Brown, P. D., Iacono, M. J., and Clough, S. A.: Radiative transfer for inhomogeneous atmospheres: RRTM, a validated correlated–k model for the longwave. *J. Geophys. Res.*, **102**, 16663–16682. doi:10.1029/97JD00237, 1997.

Mooney, P. A., Gill, D. O., Mulligan, F. J., and Bruyère, C. L.: Hurricane simulation using different representations of atmosphere-ocean interaction: the case of Irene (2011). *Atmos. Sci. Let.*, doi:10.1002/asl.673, 2016.

Mooney, P. A., Mulligan, F. J., Bruyère, C. J., Parker, C. L., and Gill, D. O.: Investigating the performance of coupled WRF-ROMS simulations of Hurricane Irene (2011) in a regional climate modeling framework. *Atmos. Res*., **215**, 57-74, 2018. https:/doi.org/10.1016/j.atmosres.2018.08.017.

Mooney, P. M., Sobolowski, S. P., and Lee, H.: Designing and evaluating regional climate simulations for land use land cover change studies at high latitudes. *Tellus A*, in review, 2020.

Nakanishi, M., and Niino, H.: An improved Mellor–Yamada level 3 model: its numerical stability and application to a regional prediction of advecting fog. *Bound. Layer Meteor.* **119**, 397–407. doi:10.1007/s10546-005-9030-8 , 2006

Nakanishi, M., and Niino, H.: Development of an improved turbulence closure model for the atmospheric boundary layer. *J. Meteor. Soc. Japan*, **87**, 895–912. doi:10.2151/jmsj.87.895, 2009

Olson, J. B., Kenyon, J. S., Angevine, W. M., Brown, J. M., Pagowski, M., and Sušelj, K.: A Description of the MYNN-EDMF Scheme and the Coupling to Other Components in WRF–ARW. *NOAA Technical Memorandum OAR GSD*, **61**, pp. 37. doi:10.25923/n9wm-be49, 2019.

Parker, C. L., Bruyère, C. L., Mooney, P. A., and Lynch, A. H.: The response of land-falling tropical cyclone characteristics to projected climate change in northeast Australia. *Clim. Dyn*., **51** (9-10), 3467-3485, https://doi.org/10.1007/s00382-018-4091-9, 2018.

Quitián-Hernández, L., González-Alemán, J. J., Santos-Muñoz, D., Fernández-González, S., Valero, F., and Martín, M. L.: Subtropical cyclone formation via warm seclusion development: The importance of surface fluxes. *J. Geophys. Res. Atmos*., https:/doi.org/10.1029/2019JD031526, 2020.

Rasmussen, R., Liu, C., Ikeda, K., Gochis, D., Yates, D., Chen, F., Tewari, M., Barlage, M., Dudhia, J., Yu, W., and Miller, K.: High-Resolution Coupled Climate Runoff Simulations of Seasonal Snowfall over Colorado: A Process Study of Current and Warmer Climate. *J. Climate*, **24** (12), 3015-3048, 2011.

Ricchi, A., Miglietta, M. M., Barbariol, F., Benetazzo, A., Bergamasco, A., Bonaldo, D., Cassardo, C., Falcieri, F. M., Modugno, G., Russo, A., Sclavo, M., and Carniel, S.: Sensitivity of a Mediterranean Tropical-Like Cyclone to Different Model Configurations and Coupling Strategies. *Atmosphere*, **8**(5), 92, https://doi.org/10.3390/atmos8050092, 2017.

Ricchi, A., Miglietta, M. M., Bonaldo, D., Cioni, G., Rizza, U., and Carniel, S.: Multi-Physics Ensemble versus Atmosphere-Ocean Coupled Model Simulations for a Tropical-Like Cyclone in the Mediterranean Sea, 2019.

784   *Atmosphere*, **10**(4), 202; https://doi.org/10.3390/atmos10040202.

785   Schär, C., Frei, C., Lüthi, D., and Davies, H. C.: Surrogate climate-change scenarios for

786   regional climate models. *Geophys. Res. Lett.*, **23**(6), 669-672, 1996.

787   Shaltout, M., and Omstedt, A., 2014. Recent sea surface temperature trends and future scenarios for

788   the Mediterranean Sea. *Oceanologia*, **56**, 411-443, https://doi.org/10.5697/oc.56-3.411.

789   Skamarock, W. C., Klemp, J. B., Dudhia, J., Gill, D. O., Barker, D. M., Duda, M., Huang, X. Y.,

790   Wang, W., and Powers, J. G.: A description of the advanced research WRF version 3. *NCAR*

791   *technical note*, NCAR/TN/u201345?STR, 123pp, 2008.

792   Somot, S., Sevault, F., and Déqué, M.: Transient climate change scenario simulation of the

793   Mediterranean Sea for the twenty-first century using a high-resolution ocean circulation

794   model. *Clim. Dyn.*, **27**, 851-879, https://doi.org/10.1007/s00382-006-0167-z, 2006.

795   Taylor, K. E., Stouffer, R. J., and Meehl, G. A.: An Overview of CMIP5 and the experiment

796   design. *Bull. Amer. Meteor. Soc.*, **93**, 485-498, doi:10.1175/BAMS-D-11-00094.1, 2012.

797   Tiedtke, M.: A comprehensive mass flux scheme for cumulus parameterization in large–scale

798   models. *Mon. Wea. Rev.*, **117**, 1779–1800,1989.

799   Thompson, G., Field, P. R., Rasmussen, R. M., and Hall, W. D.: Explicit Forecasts of Winter

800   Precipitation Using an Improved Bulk Microphysics Scheme. Part II: Implementation of a

801   New Snow Parameterization. *Mon. Wea. Rev.*, **136**, 5095–5115.

802   doi:10.1175/2008MWR2387.1 , 2008.

803   Torn, R. D.: Evaluations of Atmosphere and Ocean Initial Condition Uncertainty and Stochastic

804   Exchange Coefficients on Ensemble Tropical Intensity Forecasts. *Mon. Wea. Rev.*, **144**(9),

805   3487-3506, https://doi.org/10.175/MWR-D-16-0108.1, 2016.

806   Tous, M., Zappa, G., Romero, R., Shaffrey, L., and Vidale, P. L.: Projected changes in

807   medicanes in the HadGEM3 N512 high-resolution global climate model.

808   *Clim. Dyn.*, **47**, 1913-1924, https://doi.org/10.1007/s00382-015-2941-2, 2016.

809   Zhang, C., Wang, Y., and Hamilton, K.: Improved representation of boundary

810   layer clouds over the southeast pacific in ARW–WRF using a modified Tiedtke cumulus

811   parameterization scheme. *Mon. Wea. Rev.*, **139**, 3489–3513, 2011.

812   Zhang, W., Villarini, G., Scoccimarro, E., and Napolitano, F.: Examining the precipitation

813   associated with medicanes in the high-resolution ERA-5 reanalysis data. *Int. J. Climatol.*,
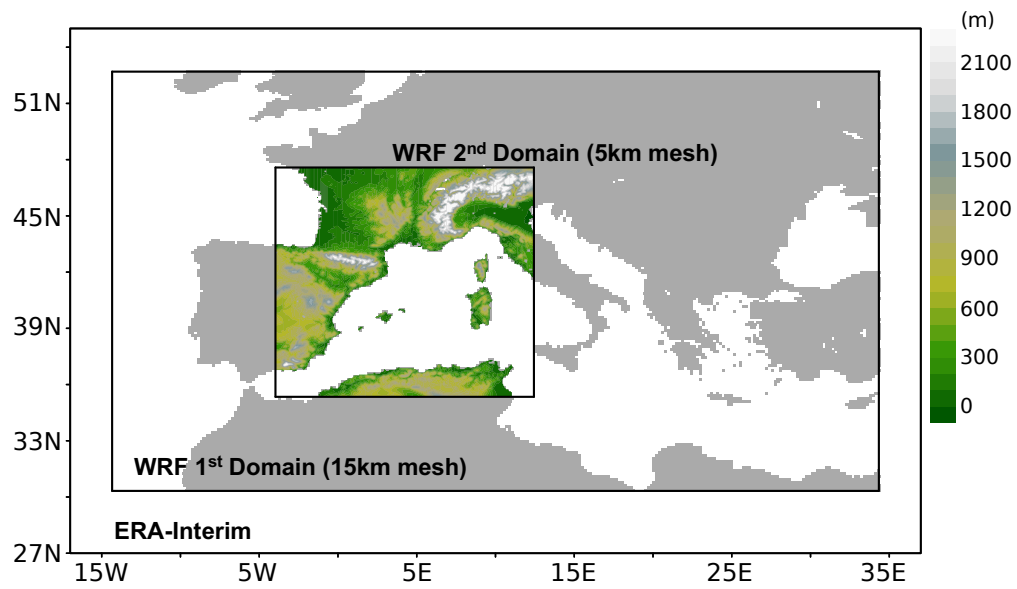
814   https://doi.org/10.1002/joc.6669, 2020.

815

816

Figure 1.
Domains for WRF simulations for medicane Rolf. Shading in WRF 2nd domain is topography height from MODIS.
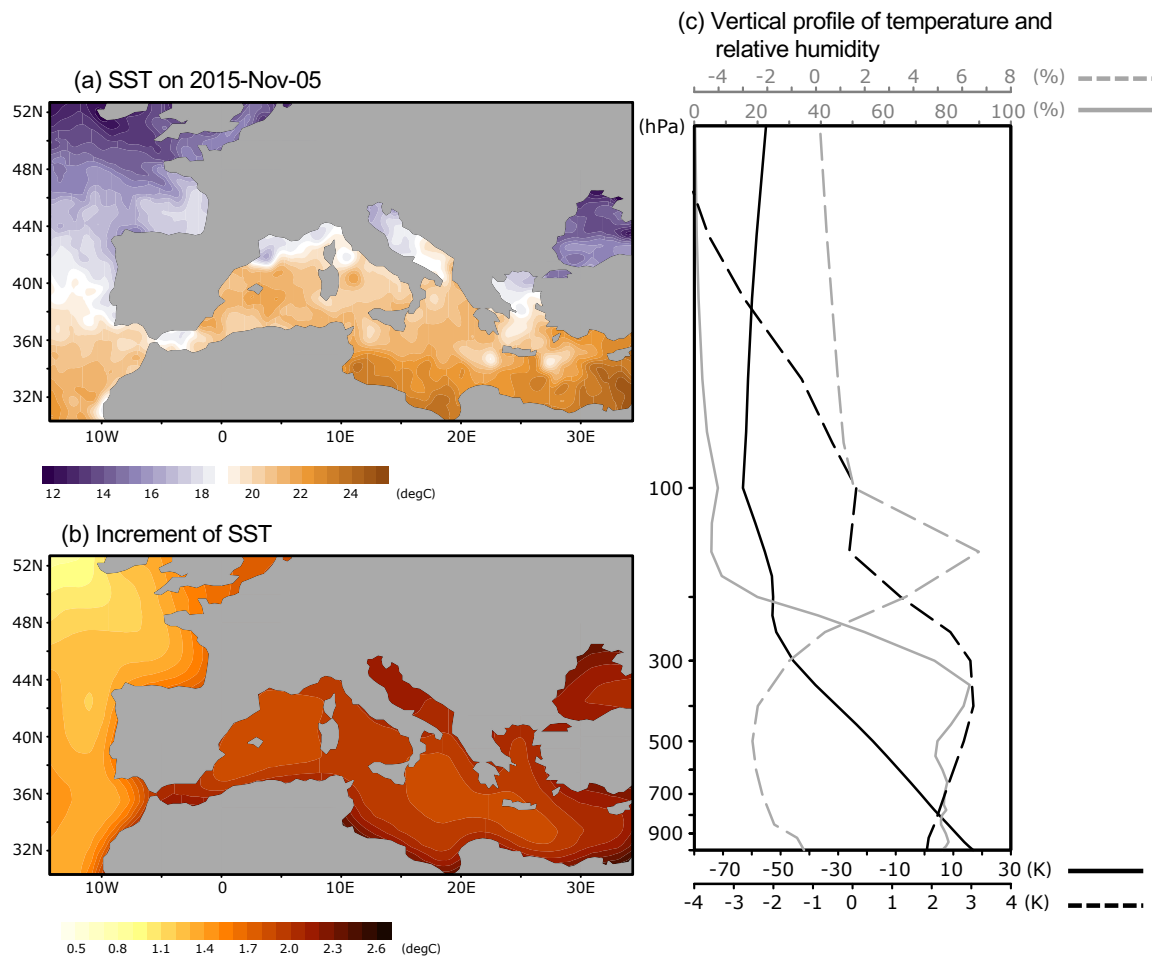
817

Figure 2.
(a) Sea surface temperature (SST) at 00UTC on 5th November, 2011 in OISST in WRF 1st domain.
(b) Increment projected by 18 CMIP5 CGCMs (b) SST in WRF 1st domain and (c) vertical profiles of increment of air temperature and relative humidity averaged over WRF's 2nd domain between 2035-2065 and 1975-2006.
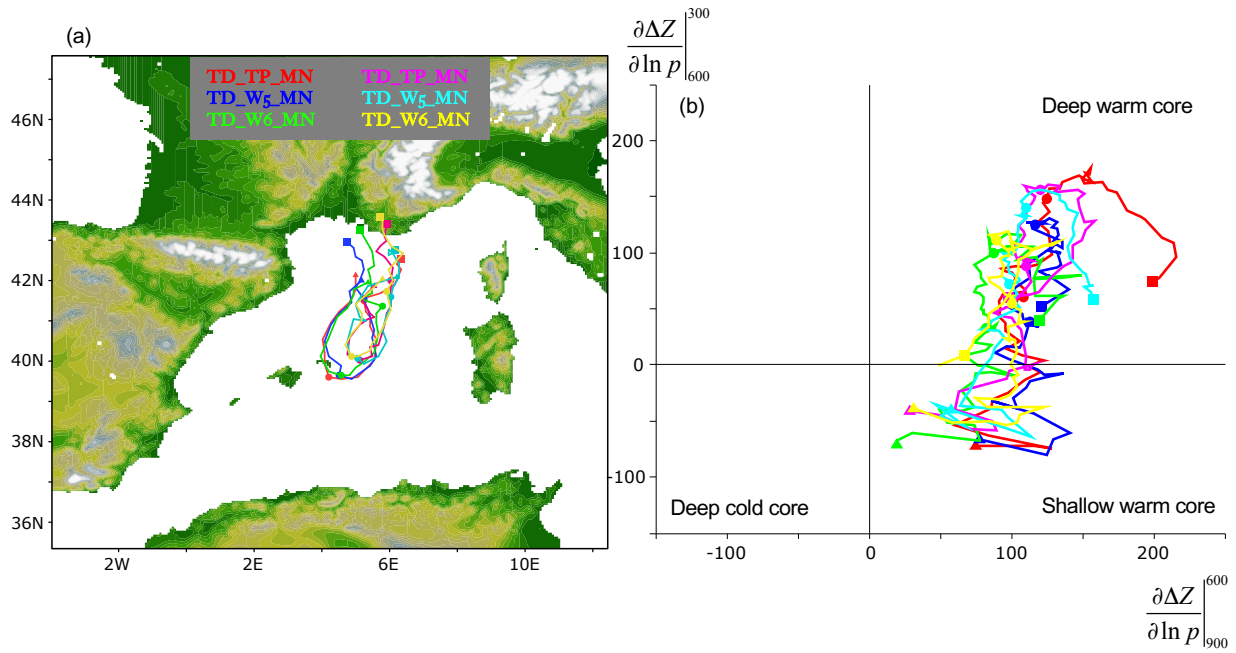
818

Figure 3.
(a) Trajectory of 6 ensembles of medicane Rolf PRS, from 00UTC, 6th, Nov, 2011 to 00UTC, 9th, Nov
The tracking is based on the lowest sea level pressure. The colors of red, blue, green, magenta, light blue, and yellow is for TD_TP_MN, TD_W5_MN, TD_W6_MN, TD_TP_MJ, TD_W5_MJ, and TD_W6_MJ, respectively. Note that the track of TD_W6_MJ (orange) terminates at 22UTC-08 due to the extinction of the simulated medicane. (b) Cyclone phase space of PRS ensemble.
The markers of ▲, ●, and ■ denote 00UTC-06, 00UTC-07/00UTC-08, and end of tracking, respectively.

819
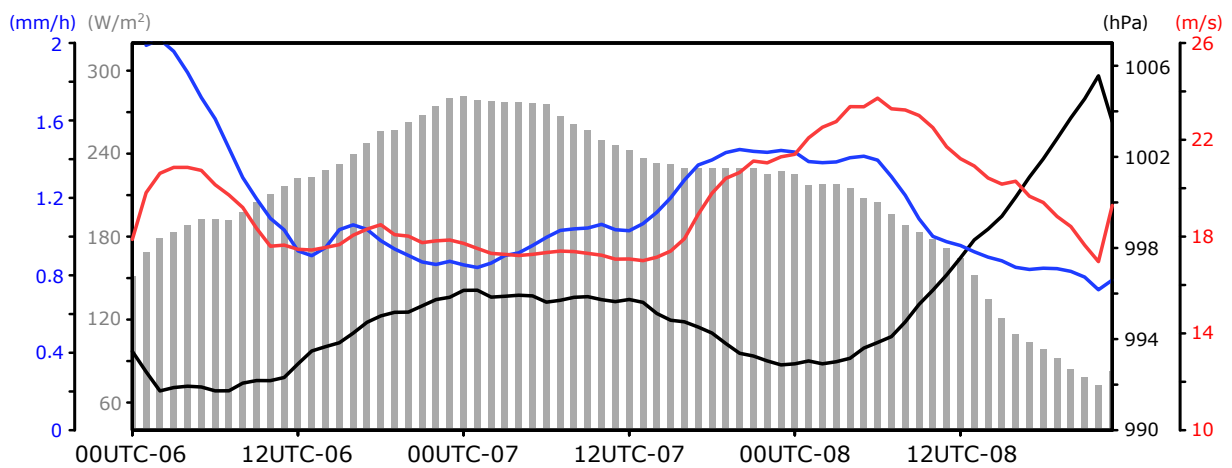
Figure 4.
Time series of sea level pressure (SLP) at grid of cyclone centre (black line), latent heat flux (grey bar),
And precipitation (blue line), and averaged wind speed exceeding 95th percentile (red line) within the
250km radius of the simulated medicane averaged within a radius of 250km.
Note that the TD_W6_MJ (orange) terminates at 23UTC-08 due to the extinction of
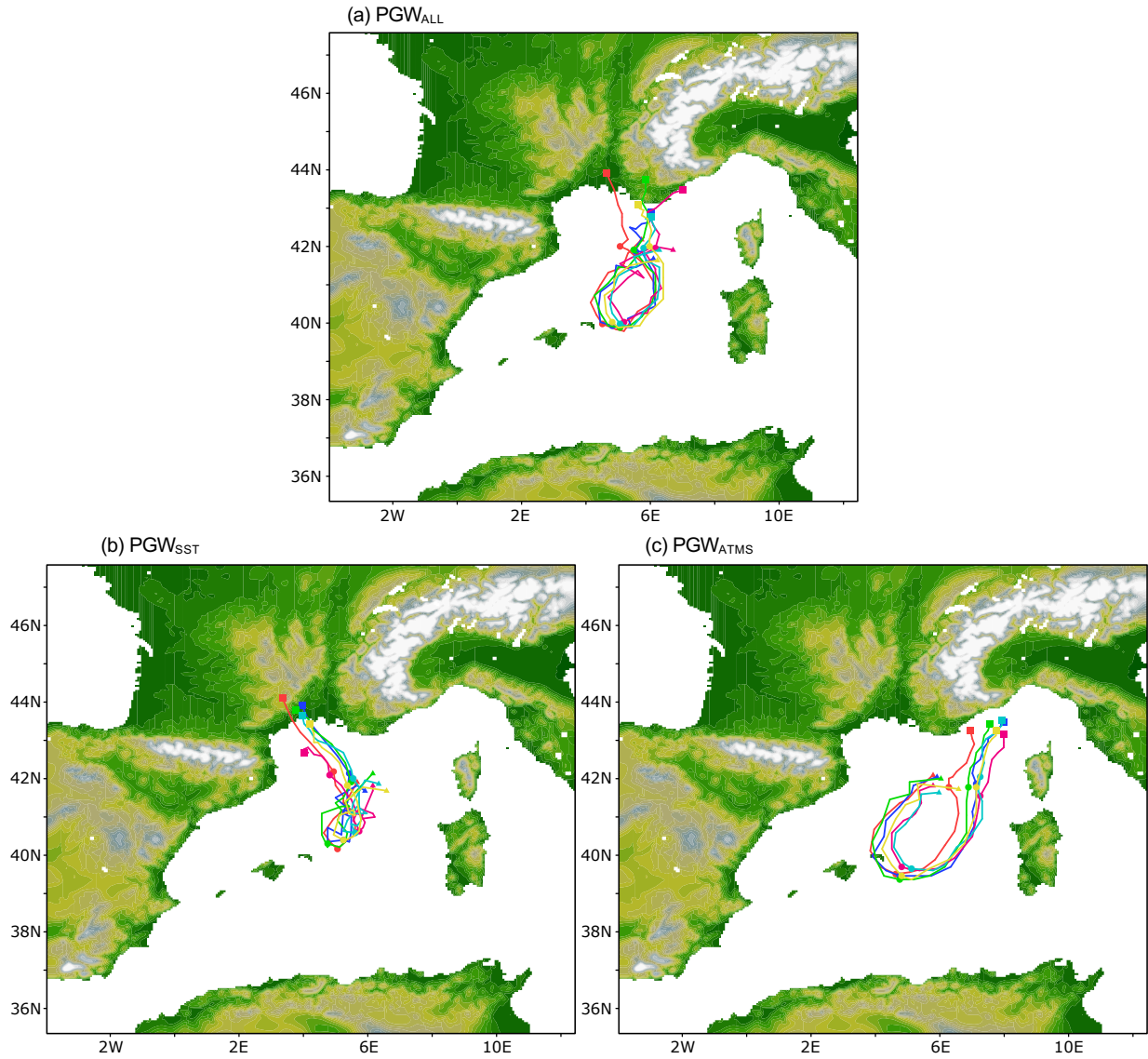the simulated medicane and the values of TD_W6_MJ iare excluded from the ensemble mean at 23UTC-08.

820

Figure 5.
Same as Fig. 3, but for (a) PGW$_{ALL}$, (b) PGW$_{SST}$, and (c) PGW$_{ATMS}$, respectively.
Note that the track of TD_TP_MN (red), TD_W5_MN (blue), and TD_W6_MN (green)
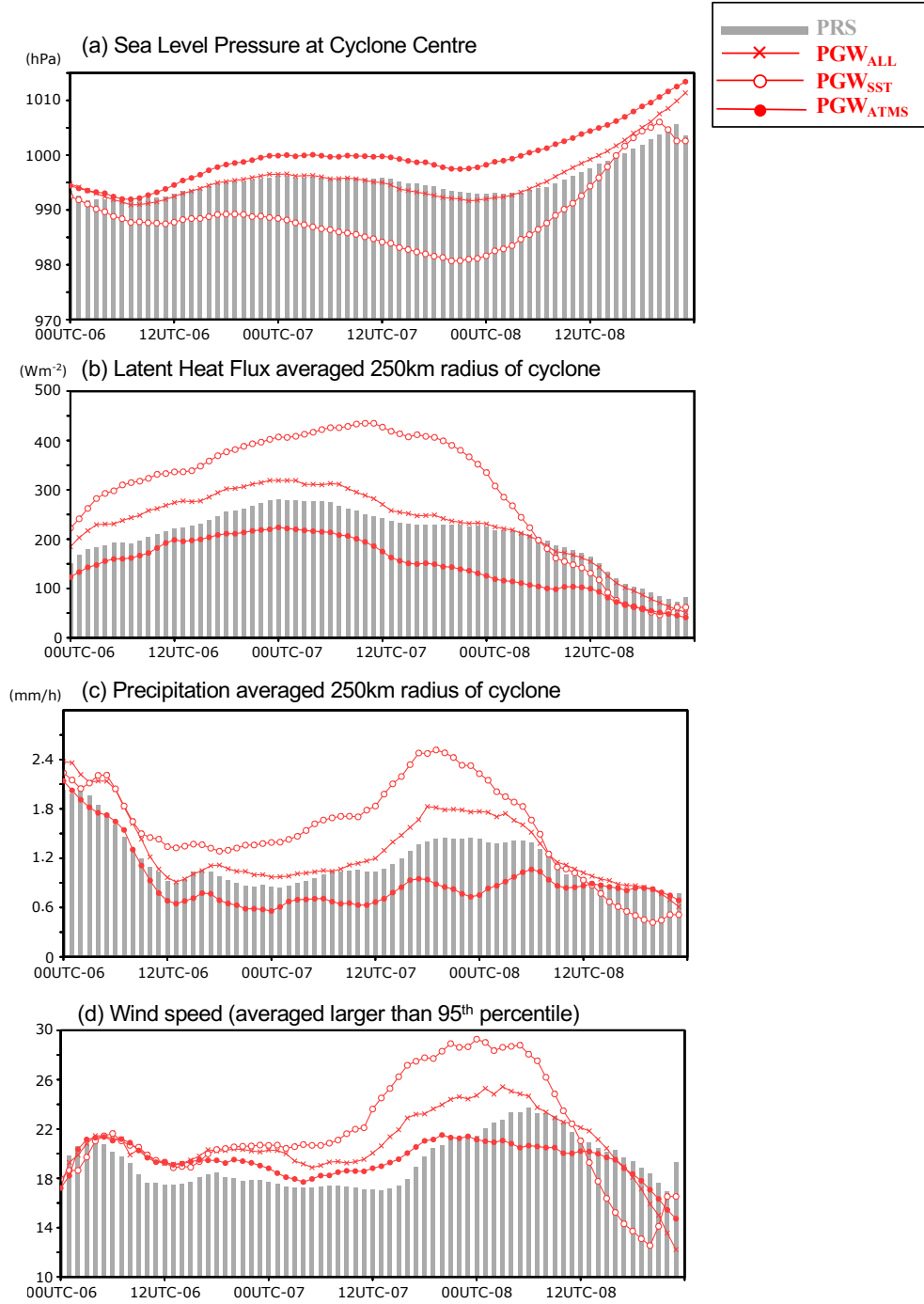in PGW$_{SST}$ terminates at 15UTC-08 due to the early landfall.

821

Figure 6.

Time series of ensemble of (a) SLP at grid of cyclone centre, (b) latent heat flux, (c) precipitation averaged, and (d) averaged wind speed exceeding 95th percentile within the 250km radius of the simulated medicane. (b) and (c) are averaged value within 250km radius The gray bar and red lines denote the variables of PRS and PGWs (with different markers), respectively. All variables are ensemble-mean. Note that the values of TD_TP_MN and TD_W5_MN in PGWSST are excluded from the ensemble mean from 2000UTC-08 and 2100UTC-08, respectively, due to the extinction of simulated medicanes.
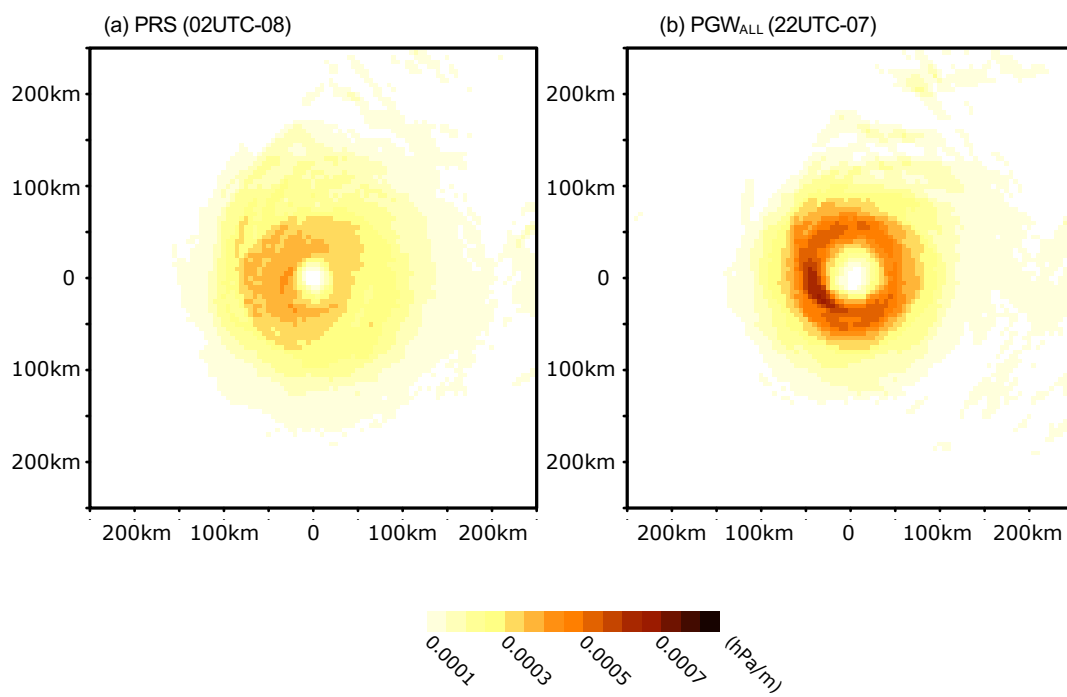
822

Figure 7.
Scalar of SLP gradient for (a) PRS and (b) PGW$_{ALL}$ around the cyclone centre at SLP minimum (referring to Fig. 6a)
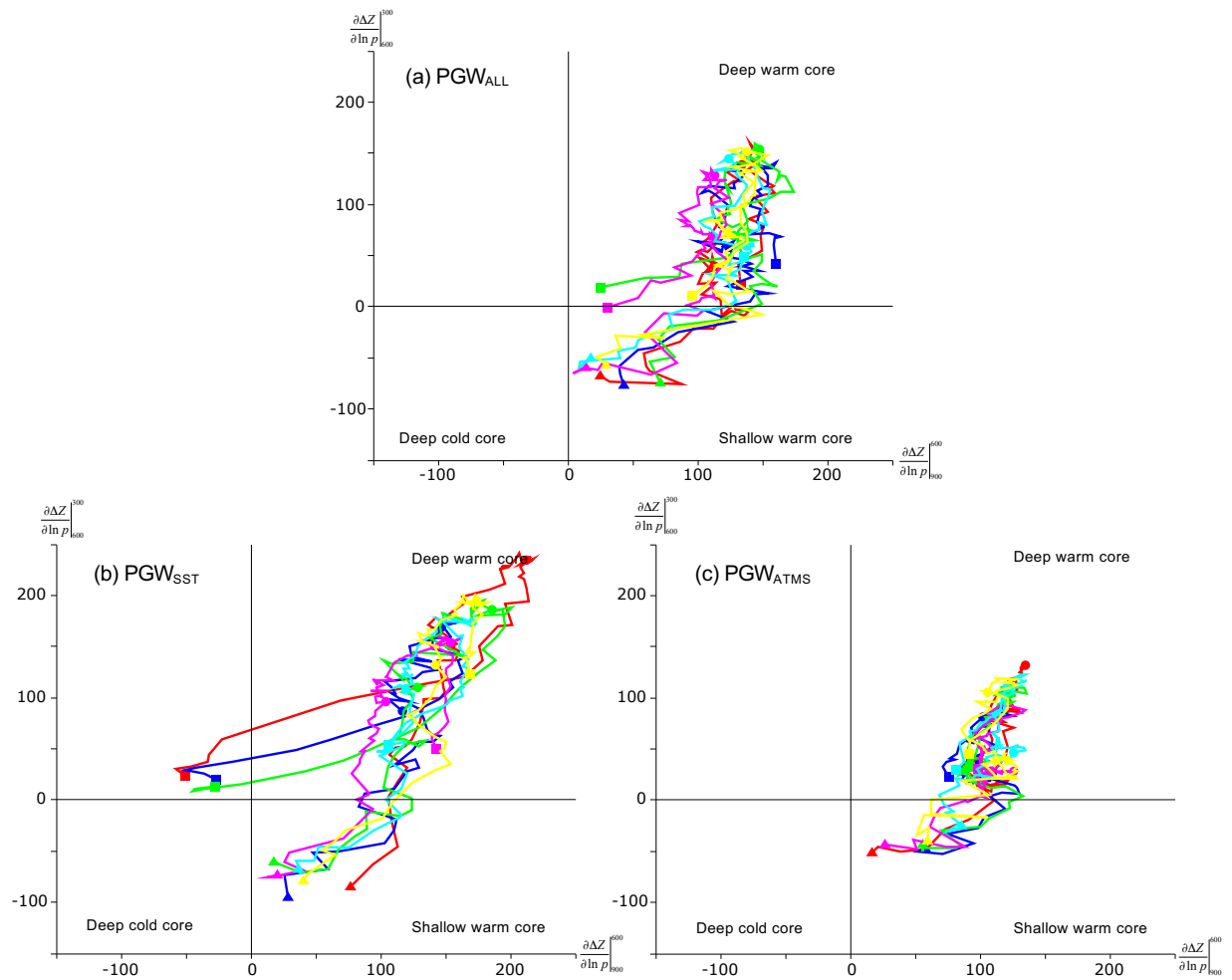
823

Figure 8.
Same as Fig. 3b, but for (a) PGW$_{ALL}$, (b) PGW$_{SST}$, and (c) PGW$_{ATMS}$, respectively.
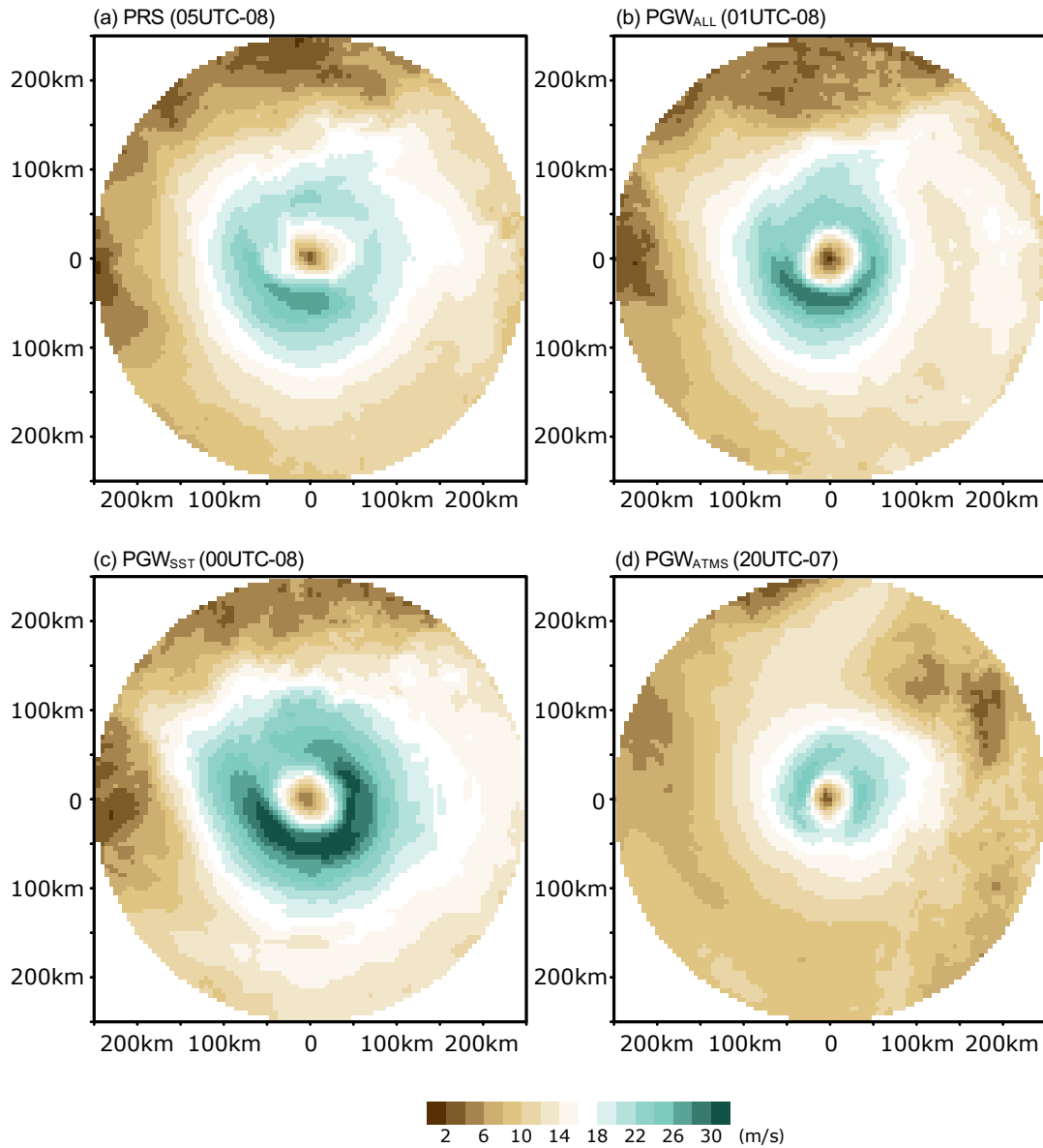
824

Figure 9.
Surface wind speed during maximum wind speed (referring to Fig. 6d) for (a) PRS, (b) PGW$_{ALL}$, (c) PGW$_{SST}$, and (d) PGW$_{ATMS}$ around the cyclone centre, respectively.
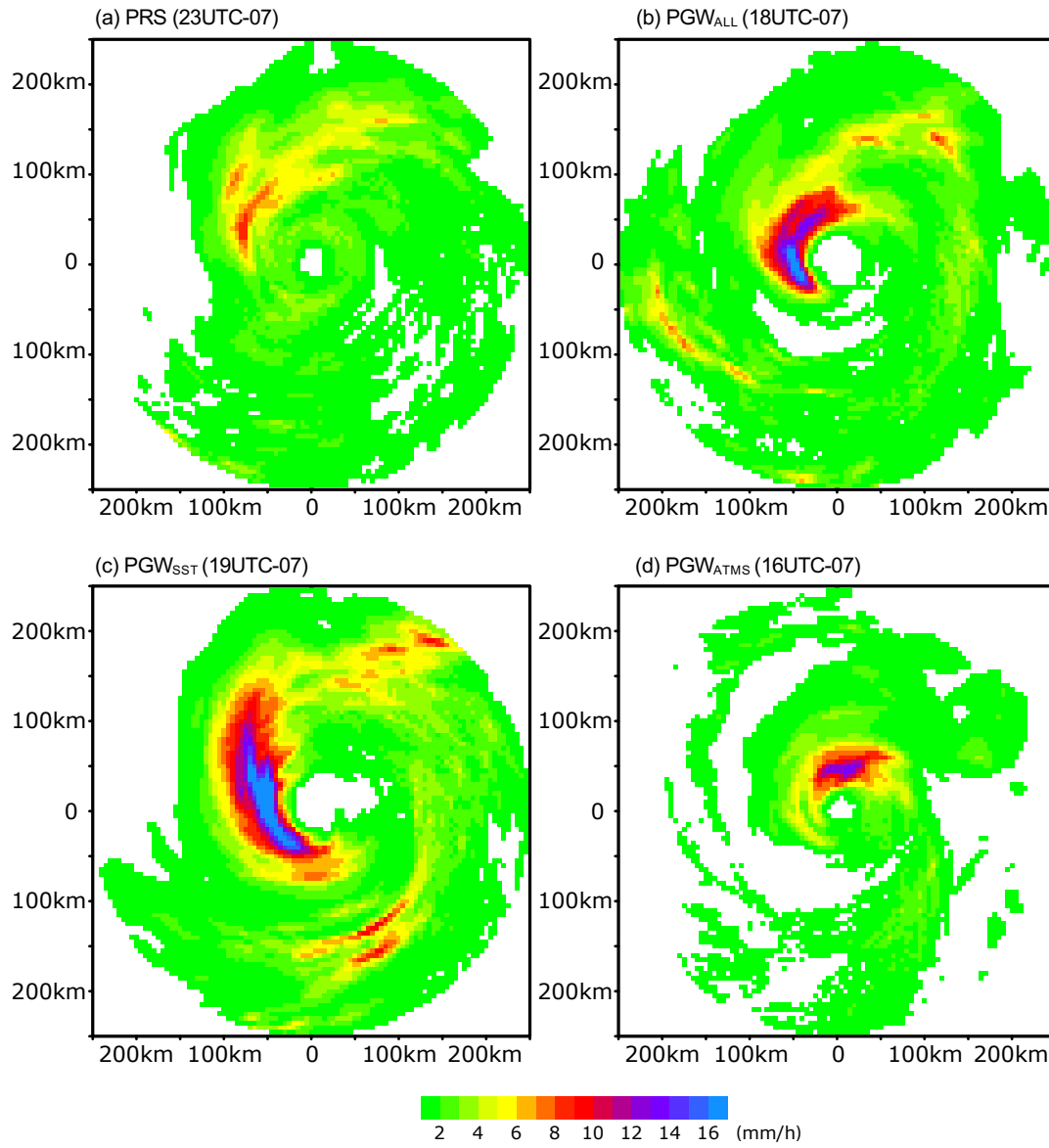
825

Figure 10.
Precipitation during its maximum (referring to Fig. 6c) for (a) PRS, (b) PGW$_{ALL}$, (c) PGW$_{SST}$, and (d) PGW$_{ATMS}$ around the cyclone centre, respectively.
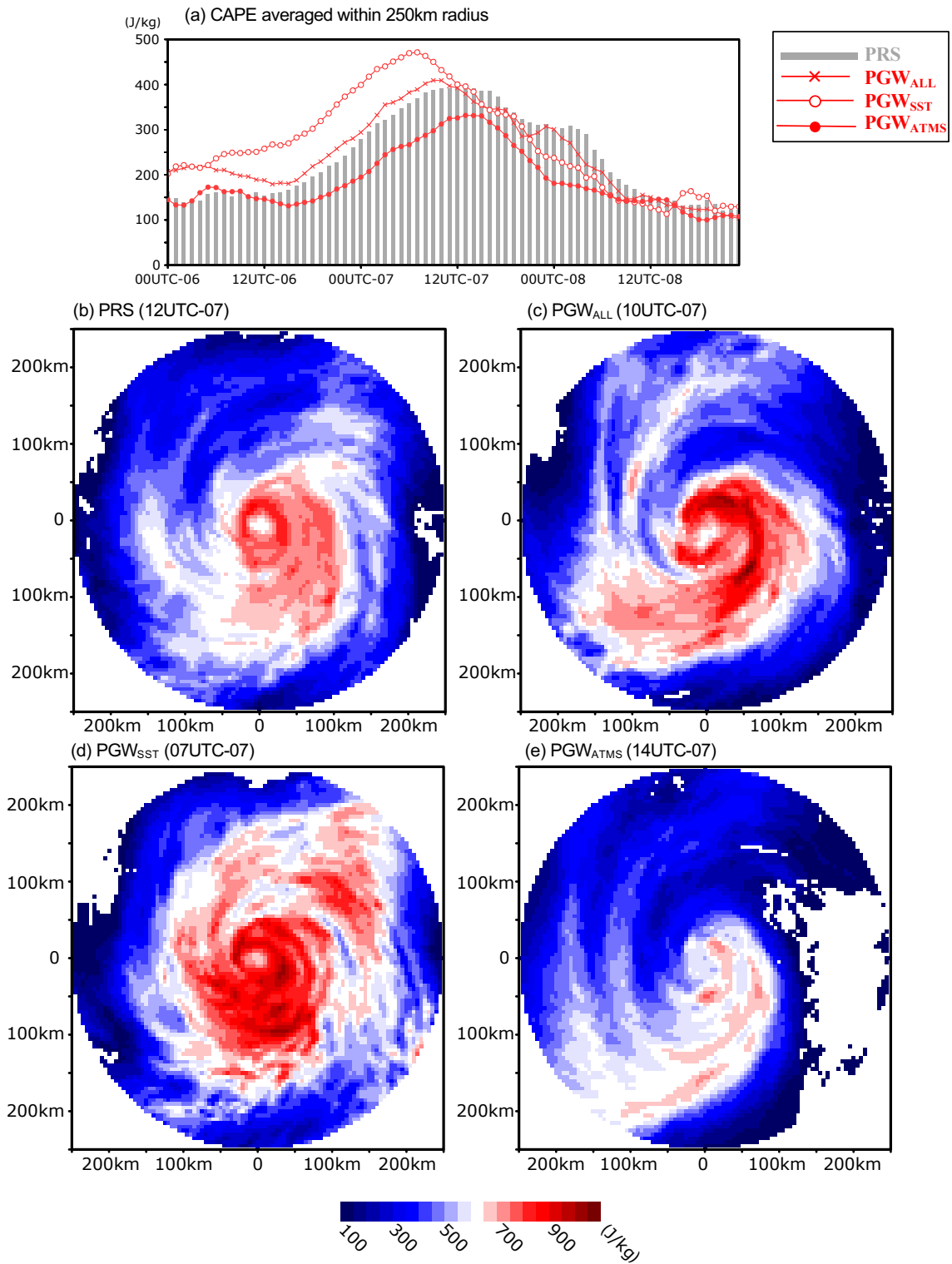
826

Figure 11.
(a) Same as Fig. 6b, but for convective available potential energy (CAPE) and CAPE at its minimum (referring to Fig. 10a) for (b) PRS, (c) PGW$_{ALL}$, (d) PGW$_{SST}$, and (e) PGW$_{ATMS}$ around the cyclone centre, respectively.

827

Figure 12.
Same as for Fig.10, but for outgoing longwave radiation (OLR)
during intense rainfall in Fig.6c

828

829   **Tables**

830

Model Name	No. Ensemble Members from Historical Simulation	No. Ensemble Members from RCP8.5 Simulation	Ensemble Members Used	Names of Member Realisations
ACCESS1-3	3	1	1	r1i1p1
CanESM2	5	5	3	r1i1p1, r2i1p1, r3i1p1
CCSM4	6	6	3	r1i1p1, r2i1p1, r6i1p1
CESM1-CAM5	3	3	3	r1i1p1, r2i1p1, r3i1p1
CMCC-CM	1	1	1	r1i1p1
CNRM-CM5	10	5	3	r2i1p1, r4i1p1, r6i1p1
CSIRO-Mk3-6-0	10	10	3	r1i1p1, r2i1p1, r3i1p1
GFDL-CM3	5	1	1	r1i1p1
GFDL-ESM2M	1	1	1	r1i1p1
GISS-E2-H	5	2	2	r1i1p1, r2i1p1
HadGEM2-CC	3	3	3	r1i1p1, r2i1p1, r3i1p1
HadGEM2-ES	4	4	1	r3i1p1
INM-CM4	1	1	1	r1i1p1
IPSL-CM5A-MR	3	1	1	r1i1p1

MIROC5	4	3	3	r1i1p1, r2i1p1, r3i1p1
MIROC-ESM	3	1	1	r1i1p1
MPI-ESM-LR	3	3	3	r1i1p1, r2i1p1, r3i1p1
MPI-ESM-MR	3	1	1	r1i1p1
MRI-CGCM3	4	1	1	r1i1p1

831

832

833 **Table 1.** CMIP5 GCMs used for deriving the climate perturbations for the PGW simulations.

834

835

	Thompson	WRF Single Moment 5 Class	WRF Single Moment 6 Class
Mellor-Yamada-Nakanishi-Niino Leve 2.5	TD_TP_MN	TD_W5_MN	TD_W6_MN
Mellor-Yamada-Janjíc	TD_TP_MJ	TD_W5_MJ	TD_W6_MJ

836

837 **Table 2.** Physical scheme combination for 6 ensemble simualtions of WRF and acronyms for each

838 simulation.

839